

ELECTROMAGNETIC PROBES OF THE HADRON-QUARK
TRANSITION IN RELATIVISTIC NUCLEAR COLLISIONS

A DISSERTATION
SUBMITTED TO THE DEPARTMENT OF PHYSICS
OF KENT STATE UNIVERSITY
IN PARTIAL FULFILLMENT OF THE REQUIREMENTS
FOR THE DEGREE OF
DOCTOR OF PHILOSOPHY

John Joseph Neumann, Jr.

May, 1996

I certify that I have read this dissertation and that, in my opinion, it is fully adequate in scope and quality as a dissertation for the degree of Doctor of Philosophy.

Professor George Fai
(Principal Advisor)

Abstract

Under ordinary conditions quarks and gluons are confined within hadrons. However, at very high temperatures and/or densities the individual quarks and gluons become free to move over distances much larger than the size of a nucleon. This phase of matter is called a “quark-gluon plasma” (QGP). Lattice Quantum Chromodynamics (QCD) calculations have predicted a transition from hadron gas to QGP at temperatures somewhere around 150 to 200 MeV. Relativistic nuclear collision experiments offer the only opportunity to study QGP in the laboratory. Quantitative details about the phase transition must be inferred from the particles leaving the small four-volume of QGP, if produced, in these collisions. It has been proposed that the transition temperature T_c can be measured by looking at the apparent temperature of the spectra of photons and leptons.

We simulate central heavy ion collisions assuming that non-viscous fluid dynamics is valid. Nuclear transparency is assumed, and an excited baryon-free region is produced between the receding nuclei. We assume in addition that at a reasonable thermalization time transverse expansion begins, coupled to the longitudinal expansion. A first-order phase transition is assumed between a massless ideal pion gas and a two-flavor quark-gluon plasma.

Photon spectra are calculated by integrating the production rate over the four-volume of the collision while taking into account the motion of the matter. Dilepton spectra from the decay of ρ^0 and ω mesons are calculated in a very similar manner by using the product of the ρ^0 and ω distributions and decay rates.

It is shown that the apparent temperatures of the spectra are sensitive to the T_c used in the simulations. The availability of photon and dilepton spectra from the European CERN/SPS allows us to constrain T_c and other parameters of the model. The main conclusion of this work is that electromagnetic probes can be used as a thermometer for the hadron-quark transition temperature with judicious choice of the experimental conditions.

Acknowledgements

I would like to thank my advisor, Dr. George Fai, for all his encouragement and direction. Not only has he been a great teacher, but a good friend to me. Also, for good or bad, he convinced me to become a theorist, something that I now feel I was meant to be. Dr. David Seibert also deserves much thanks— he has been almost a co-advisor during parts of this work, and also a great source of motivation.

Mr. Bob Sorensen, at Springville-Griffith Institute Central High School, and Dr. Jonathan Reichert, at the State University of New York at Buffalo, were the first people to make me realize that physics is really a fun subject when you have a good teacher. I'd like to thank them for turning me in the direction of being a starving physicist rather than a starving musician.

I would like to thank my fiancée Barbara for all her love and patience while I worked on this.

Most importantly, I want to thank my parents and family. They knew what I could do, and made sure I did. Thanks.

Contents

Abstract	iii
Acknowledgements	iv
1 Introduction	1
2 Fluid Dynamics	7
2.1 Description of Collision Geometry	7
2.2 Equation of State	13
2.3 Estimating Initial Conditions	17
2.4 The Godunov Method	18
2.5 Similarity Solutions	21
2.6 Fluid Dynamics Code	26
2.6.1 Subroutine <i>edgevalue</i>	27
2.6.2 Other Subroutines	36
2.7 Fluid Dynamics Results	38
3 Photon Production	47
3.1 Space-Time Evolution of Photon Production	47
3.2 Photon Production Rates	49
3.3 Results	50
4 Electron-Positron Pairs	58
4.1 Dilepton Production from Thermal Resonances	58
4.2 Electron-positron Production from Equilibrium Matter	61
4.3 e^+e^- Pairs from Freeze-out	62

4.3.1	Freeze-out with No Transverse Expansion	64
4.4	Simulating Experimental Cuts	65
4.4.1	Cut in Invariant Mass	65
4.4.2	Cut in Rapidity	66
4.4.3	Cut in Opening Angle	67
4.5	Apparent Temperature of Dilepton Spectrum	67
4.6	Results	68
5	Conclusions	72
A	Fluid Dynamic Details	75
A.1	Shocks and Stability	75
A.2	Rarefaction Waves	77
B	Math: Equation of State	80
B.1	Entropy of Pions	80
B.2	The 7/8 Factor	81
C	Math: Miscellaneous	83
C.1	Corrections to Pressure Estimate	83
C.2	Interpretation of Roots of Eq. 4.4	84
	Bibliography	89

List of Figures

1.1	Schematic evolution of the temperature with first-order phase transition. . .	3
2.1	The Bjorken picture	8
2.2	Rapidity distribution of matter	10
2.3	Cylindrical geometry of system	12
2.4	Joining two regions of pure phase matter	24
2.5	Joining a mixed phase region with the vacuum	25
2.6	Cases 1 & 6: Joining regions of pure phase	28
2.7	Cases 2 & 3: Joining quark phase matter with mixed phase matter	30
2.8	Case 4: Joining two mixed phase regions	32
2.9	Case 5: Joining mixed phase matter with pure hadronic matter	33
2.10	Case 7: Joining quark matter to the vacuum	34
2.11	Case 8: Joining mixed phase matter to the vacuum	35
2.12	Case 9: Joining hadronic matter to the vacuum	37
2.13	Profiles of w and v for S+Au, with standard set, $dN/dy = 225$, and $T_c = 150$ MeV	39
2.14	Same as Fig. 2-13, with $T_c = 170$ MeV	41
2.15	Same as Fig. 2-13, with $T_c = 200$ MeV	42
2.16	Profiles for $\tau_0 = 1$ fm, $T_c = 150$ MeV	43
2.17	Profiles for $f = 0.7$, $T_c = 150$ MeV	44
2.18	Profiles for Pb+Pb ($dN/dy = 1200$) and $T_c = 150$ MeV	45
2.19	Profiles for S+Au with $dN/dy = 188$ and $T_c = 150$ MeV	46
3.1	Photon spectra in a central S+Au collision at SPS energy	51
3.2	T_{fit} vs. T_c for photons	52
3.3	Preliminary WA80 data and selected fits	54

3.4	Predicted photon spectra for central Pb+Pb collisions at SPS energy	56
4.1	Invariant mass spectrum of e^+e^- pairs	59
4.2	Freeze-out schematic	63
4.3	Typical e^+e^- m_T -spectra	69
4.4	Apparent Temperatures	70
C.1	When there is exactly one solution for p_*	86
C.2	When there are two solutions for p_*	87

Chapter 1

Introduction

What is stuff made of?

Since the time of the ancient Greeks, and probably before, people have been asking this question; the same question intrigues children and many scientists to date. As children, we usually got the answer in terms of things that are visible to the naked eye, e.g. “that piece of cloth is made out of threads.” For the ever-inquisitive child, and those of us who have yet to outgrow this basic curiosity, the question still remains: what are the threads made of? What is the stuff that makes up the threads made of? and so on, down to the things that are not made of anything simpler. These *elementary constituents* of matter have been believed to be various things through the ages, becoming more elementary in the course of history: fire, earth, wind and water; chemical compounds (molecules); atoms and ether; nuclei and electrons; protons and neutrons (and a little later, many other species of hadrons); and at present, quarks, leptons, and massless gauge particles such as photons and gluons.

From the point of view of experiment, it is necessary to use higher and higher energies to acquire the resolution necessary to experience or infer the existence of these smaller and smaller constituents. The chain of inference has also grown longer at each level. Indeed, scattering experiments, which are used as tools for understanding what is happening inside the nucleus, have been likened to smashing a watch and understanding how it operated by observing how the pieces fly out. As hopeless as this sounds, it is possible to obtain information about the fundamental forces by taking measurements from a large number of

collision events and comparing the data with model predictions.

The primary goal of this work is to provide a technique for measuring the transition temperature between a gas of hadrons, and a phase of matter comprised of “free” quarks and gluons. It is believed, based on the Standard Model, that quarks do not exist freely; they are confined. At very high temperatures (>150 MeV) [1] or densities (5-10 times standard nuclear density, $\rho_0 = 0.17 \text{ fm}^{-3}$) [2] they become deconfined, meaning that while they still cannot be seen in isolation, they melt into a plasma wherein they move distances large compared to the size of a nucleon (≈ 1 fm). At normal temperatures and densities, the color forces (forces due to the “color charges” that quarks and gluons carry, analogous to electrical charges) bind the quarks into pairs (mesons) or triplets (hadrons) with no net color. It is of great interest whether we can produce the high-temperature phase of matter, the “Quark Gluon Plasma” (QGP), in the laboratory by colliding large nuclei at high energies. There is no clearer evidence of the strong interest of the community than the experiments devoted to relativistic nuclear collisions at the Alternating Gradient Synchrotron (AGS) and Super Proton Synchrotron (SPS) accelerators and the experimental programs planned for the Relativistic Heavy Ion Collider (RHIC) and Large Hadron Collider (LHC). This is a very exciting time, as preliminary results are starting to emerge from SPS, and we take this opportunity to compare our results to the data.

It is generally believed that, as discussed above, at sufficiently high energy densities a transition occurs to a high-energy phase in ultrarelativistic nuclear collisions. We adopt this position here and, accordingly, assume the existence of some kind of a transition to a quark-gluon plasma (QGP). We are interested in the transition temperature and in the nature of the transition. We are mostly limited to parametrizing the properties of the transition, and for this work, we assume a first-order phase transition. The time-evolution of the temperature, for a uniform longitudinally expanding system, is shown in Fig. 1.1. Our emphasis is not on comparing different scenarios with and without a transition; rather we will vary the parameters of the model in order to investigate the possibilities of experimentally measuring the transition temperature. We focus on electromagnetic particles, such as real photons and lepton pairs, as they have long mean free paths in hadronic matter, and are therefore well suited for studying the earliest (hot and dense) stages in the evolution of the hot matter produced in ultrarelativistic nuclear collisions.

How can one measure the transition temperature using electromagnetic probes? If the system, during its evolution, spends a significant amount of time at a given temperature,

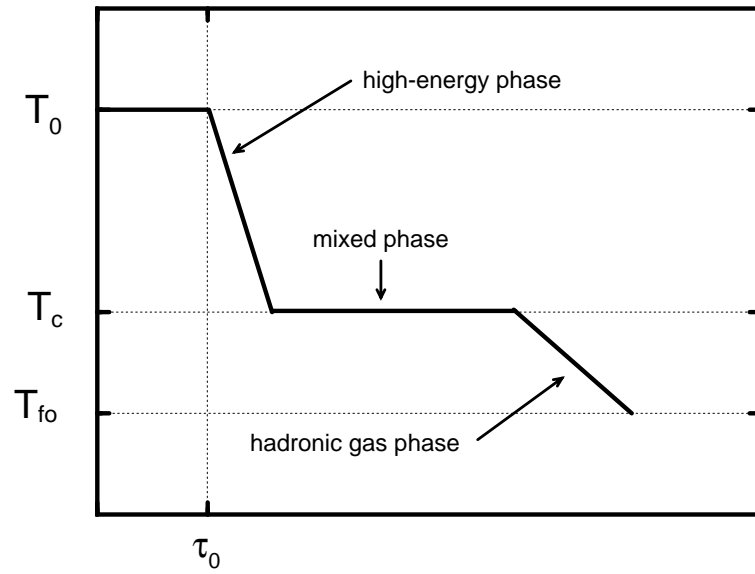


Figure 1.1: Schematic evolution of the temperature as a function of proper time in the central region of a relativistic nuclear collision system when the EOS contains a first-order phase transition. T_0 , T_c , and T_{fo} refer to the initial, critical, and freeze-out temperatures, respectively, and τ_0 is called the thermalization time.

then a large fraction of the produced photons and lepton pairs will be emitted during that time and their spectra can be expected to reflect that temperature. So the strategy is to plot the spectra as a function of transverse momentum for photons $p_T = \sqrt{p_x^2 + p_y^2}$ (the \hat{z} axis is the beam direction) or transverse mass $m_T = \sqrt{m^2 + p_T^2}$ (for dileptons), and to read off an effective temperature or fit temperature, T_{fit} , if indeed these spectra can be approximated thermally, i.e. with an exponential fit. Then, using a model, one wants to study how the fit temperature T_{fit} is correlated to the transition temperature. As we will see, the spectra are generally almost exponential. This is illustrated by recent preliminary WA80 data for photons [3], which we will use for comparison to our calculated results. The preliminary NA45/CERES data for e^+e^- pairs [4] are not sufficiently detailed to contain transverse mass spectra; we will compare to their total production cross section in the $\rho - \omega$ peak. We will also see that, even though the physics is significantly more complicated than the expectation described above, features of the $T_c - T_{fit}$ correlation survive modeling of processes like transverse expansion and freeze-out, so that useful constraints can be placed on T_c from the data.

One of the difficulties presented by the above suggestion is the background production of photons and lepton pairs. There are many different sources of background that we will not discuss here. However, the presence of vector-meson peaks in the lepton-pair spectra gives us an opportunity to concentrate on invariant mass regions where most of the pairs come from the decay of these resonances. In this work, we focus on the least massive of the vector-meson resonances, the $\rho - \omega$ peak. Choosing the p_T and m_T windows with care provides another way to fight the backgrounds. We could have calculated $\mu^+\mu^-$ pairs instead of e^+e^- pairs, but the e^+e^- pairs were chosen because the available experimental data come from S+Au collisions at the same energy as in the WA80 experiment, making comparisons between the two more meaningful.

For our calculation, we need two basic ingredients: (i) a description of the space-time history of the collision and (ii) emission rates at a given temperature, so that the signal can be integrated over the evolution of the collision system. We will take the rates from the literature and concentrate on the description of an ultrarelativistic collision of heavy nuclei in what follows. We use standard high-energy conventions, $c = \hbar = k_B = 1$.

In this dissertation, we study the production of thermal photons and of e^+e^- pairs from thermal resonances in the central rapidity region of S+Au and Pb+Pb collisions

at SPS energy. I have written a boost-invariant one-dimensional (cylindrically symmetric) fluid dynamics code to achieve this goal. The system is assumed to be in thermal equilibrium throughout, while deviations from chemical equilibrium are considered in a parametrized form. It is assumed that the system expands radially away from the beam axis in a cylindrically-symmetric manner. We use equations of state with a first-order transition between a massless pion gas and a high-energy phase with transition temperatures in the range $150 \text{ MeV} \leq T_c \leq 200 \text{ MeV}$.

This dissertation is organized as follows. Chapter 2 is about fluid dynamics. In it I explain how the temperature and radial velocity of the hot QGP and hadronic matter are calculated for the course of the collision. The assumptions used in the model are described in Section 2.1, which describes the collision geometry and the geometry of the produced hot matter in the central region. This is followed by a section describing the equation of state (Sect. 2.2) used in all the calculations, and a section on estimating initial conditions (Sect. 2.3). The Godunov method, which is used to calculate the fluid dynamics, is explained, followed by a section about the similarity solutions (Section 2.5) which are used by the Godunov method to calculate inter-cell flow. After the basic theory of the fluid dynamics and the Godunov method, a detailed description of my fluid dynamics code is provided in Section 2.6. At the end of the chapter (Sect. 2.7), illustrative results of the fluid dynamics code are provided.

Chapter 3 shows how single photon spectra are calculated given the temperature and velocity information from the fluid dynamics code. In Section 3.1, the basic math is worked out for calculating the transverse-momentum spectrum produced during the evolution of the collision. In Section 3.2 the photon production rates are discussed, and I show how we used them. Finally, the results of the calculations are given (Section 3.3) and compared to preliminary data from the CERN WA80 experiment.

Chapter 4 is similar in structure to Chapter 3. In Section 4.1, the basic math is worked out for calculating the transverse-mass spectrum of e^+e^- pairs produced during the evolution of the collision. There are two types of contributions for the e^+e^- pair production, pairs from thermally equilibrated matter and pairs from freeze-out (Sections 4.2 and 4.3). There is a discussion of some of the finer points of evaluating the integrals in the Appendix (Sect. C.2). Descriptions of the cuts used in the NA45 experiment are provided in Sect. 4.4. The next section, Sect. 4.5 describes how the data are fitted with a temperature. Finally, the results of the calculations are displayed (Section 4.6), along with preliminary data from

the NA45/CERES experiment.

The appendices provide detailed discussions which would have interrupted the flow of the text. Appendix A provides the derivation of shock condition equations (Sect. A.1) and the differential equation describing smooth rarefaction waves (Sect. A.2). Appendix B provides derivations of the entropy per pion (B.1) and the seven-eighths factor (B.2) that are alluded to in the text of Sections 2.2 and 2.3. Section C.1 shows the effect of refinements in the estimation of the time-averaged pressure, discussed in Sect. 2.4, and a discussion (Sect. C.2) on inverting the Lorentz transform of Sect. 4.1.

There is one final note about the terminology used in this work: I often use the term *center of mass* (CM) frame, referring to the center of mass of the colliding nuclei. This is in contrast to the *fluid rest frame*, which travels outward radially with the hot matter. The calculated spectra are supposed to simulate the observed spectra at mid-rapidity, i.e. the CM frame, where the baryon-free approximation is most valid. As rapidity (see Sect. 2.1) is arbitrary with respect to an additive constant, we choose mid-rapidity (and the CM frame) to be $y = 0$.

Chapter 2

Fluid Dynamics

In Chapters 3 and 4 we will calculate the spectra of electromagnetically produced light particles emerging from high-energy heavy-ion collisions. Assuming that one knows both the state of the matter (i.e. the temperature and velocity) at each time and place, as well as the production rates for any given temperature, one may convolute these together to find the total spectrum from the collision event. This chapter deals with calculating the temperature and velocity throughout the evolution of the hot matter (which is treated as a one-component fluid for fluid dynamical purposes), starting from its initial hot compressed state immediately after the time of maximum overlap. In Section 2.1 the geometry of the colliding system is described. In Section 2.2, I describe the equation of state used for our calculations, and in Section 2.3 I show how to estimate the initial conditions. In Section 2.4, the Godunov method for fluid dynamics is described; the flow patterns are discussed in Section 2.5. Finally, in Section 2.6, there is a detailed description of how the fluid dynamics code works, along with some graphs showing the results. The FORTRAN source code is available at <http://cnr2.kent.edu/~neumann>.

2.1 Description of Collision Geometry

Before time $t = 0$ in the center of mass (CM) frame, the two heavy nuclei travel towards each other along the beam axis (which we take to be the \hat{z} -direction) with a total energy of $\sqrt{s} = 20$ GeV/nucleon. At this energy, the colliding nuclei are Lorentz-contracted (by a factor of 20 in the CM frame, 900 for the projectile in the lab frame) into nuclear “pancakes”, as illustrated in Figure 2.1 [5]. For simplicity, and for comparison to high-multiplicity

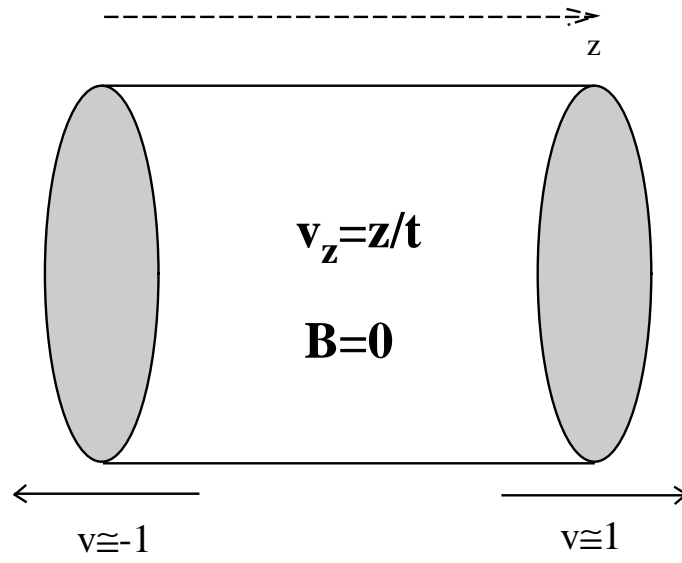


Figure 2.1: The Bjorken picture.

experiments, we concern ourselves only with central and near-central collisions. At time $t = 0$ the two nuclei reach $z = 0$, the point of maximum overlap. Because there is only partial stopping in this energy range [2], the pancakes pass through each other leaving behind an excited region at central rapidity which we model as boost-invariant (along the beam axis) and baryon-free. By boost-invariant I mean that the physics is invariant with respect to a velocity boost in the \hat{z} -direction. It is this boost-invariance that allows us to assume that at an arbitrary position z along the beam axis (in between the receding nuclei) the physics in that slice of the hot matter proceeds in the same way, as a function of the slice's proper time $\tau = \sqrt{t^2 - z^2}$, as the physics in any other slice. The zero baryon number in the central region is an approximation based on experimental observation [6].

Rapidity, defined as $y \equiv \text{arctanh}(v_z)$, is a quantity which has the useful property of being relativistically additive, in analogy to ordinary velocity in non-relativistic physics, so that we may obtain the rapidity in a different frame by simply adding a constant rapidity shift. We conventionally take $y = 0$ to be the rapidity of the CM frame. At the energy mentioned above, the projectile and target nuclei are initially separated by a rapidity difference of about $\Delta y = 7.5$. After the collision (see Figure 2.2), each nucleus loses about one unit of rapidity [2]. We call the region around $y = 0$, extending about a half unit of rapidity either way, the mid-rapidity region. The rapidity range between the receding nuclei, $-2.75 < y < 2.75$ ($0 < y < 5.5$ in the lab frame), is called the central-rapidity region [2], and we assume it evolves according to the picture described by Bjorken [5]. In this picture, the space-time rapidity of the excited central region follows a scaling behavior, i.e. $v_z = z/t$, where v_z is the velocity of the fluid along the beam axis, z is the distance along the beam axis, and t is the time since maximum overlap of the colliding nuclei, all as observed in the CM (zero-rapidity) frame.

At a certain proper time $\tau = \tau_0$, (typically 0.2 fm) [7, 8] the matter is assumed to reach thermal equilibrium, and we replace the pure longitudinal expansion of the Bjorken picture with transverse expansion coupled to the boost-invariant longitudinal scaling. The entropy density of the hot matter at τ_0 is calculated by assuming that the evolution is isentropic (because it is a free expansion into a vacuum), and that the observed pion multiplicity per unit rapidity dN_π/dy is proportional to the entropy per unit rapidity at the end of the collision. The longitudinal boost-invariance implies that the transverse expansion proceeds in the same way in each fluid rapidity slice $dy_f = dz/(\tau \cosh y)$; the volume per unit rapidity of the hot matter at $\tau = \tau_0$ and $y = 0$ (mid-rapidity) is $V = \pi R^2 \tau_0$ where R is the radius

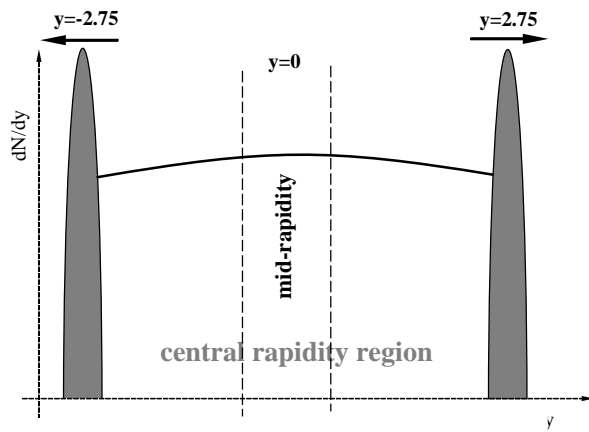


Figure 2.2: Rapidity distribution of matter, viewed in the center of mass frame of a $\sqrt{s} = 20$ GeV heavy ion collision.

of the smaller of the two nuclei. For proper time $\tau > \tau_0$, we calculate the radial flow of the fluid at $y = 0$ as a function of the radius r and the proper time τ .

Because we have a cylindrically-symmetric and boost-invariant system, the transverse expansion is completely described by specifying the enthalpy density w (energy density e + pressure P , measured in the rest frame of the fluid) and radial fluid velocity v as a function of proper time τ and radial distance r . The temperature of the fluid as measured in its rest frame can be calculated from w using the equation of state (see Sect. 2.2). The state of the fluid is most easily expressed in terms of the relativistically covariant energy-momentum tensor $T^{\mu\nu} = (e + P)u^\mu u^\nu - P g^{\mu\nu}$, with e being the energy density, P the pressure, u the four-velocity, and $g^{\mu\nu} = \text{diag}(1, -1, -1, -1)$ the metric tensor. Given an equation of state and the assumption of ideal (non-viscous) fluid flow, we can calculate the fluid dynamic behavior from the conservation law $\partial_\mu T^{\mu\nu} = 0$. Our system is cylindrically symmetric, so we would like to rewrite the conservation laws in terms of the appropriate energy-momentum tensor elements,

$$\begin{aligned} T^{00} &= w\gamma^2 - P \\ T^{r0} = T^{0r} &= wv\gamma^2 \\ T^{rr} &= wv^2\gamma^2 + P \end{aligned} \tag{2.1}$$

where v and $\gamma^2 = (1 - v^2)^{-1}$ refer to the radial fluid velocity. We do this by taking the expressions in Cartesian coordinates, and manually taking into consideration the cylindrical geometry and longitudinal boost invariance.

Consider our cylindrically-symmetric system. We are interested in rewriting the divergence at a point in the CM frame $(t, x, y = 0, z = 0)$, where t is the time, x is the distance from the axis of the cylinder, z is the distance along the axis of the cylinder (the beam direction), and y is orthogonal to both x and z (see Fig. 2.3). Thus without loss of generality we will identify x with the radial coordinate r when we express this in cylindrical coordinates. If v is the radial velocity at $(t, x, 0, 0)$ we may write $v_x = v \cos \phi$, $v_y = v \sin \phi$ for the fluid in the immediate vicinity of $(t, x, 0, 0)$, where ϕ is the angle between the velocity vector and the x -axis. Because we are interested in first derivatives only, it is sufficient to expand the trig functions to first order in the infinitesimal displacement y : $\cos \phi = 1$ and $\sin \phi = \phi = \tan \phi = y/x$. Furthermore, the boost-invariance means that $v_z = z/t$.

We write out the two Cartesian equations with $\nu = 0, 1$, inserting the above expressions

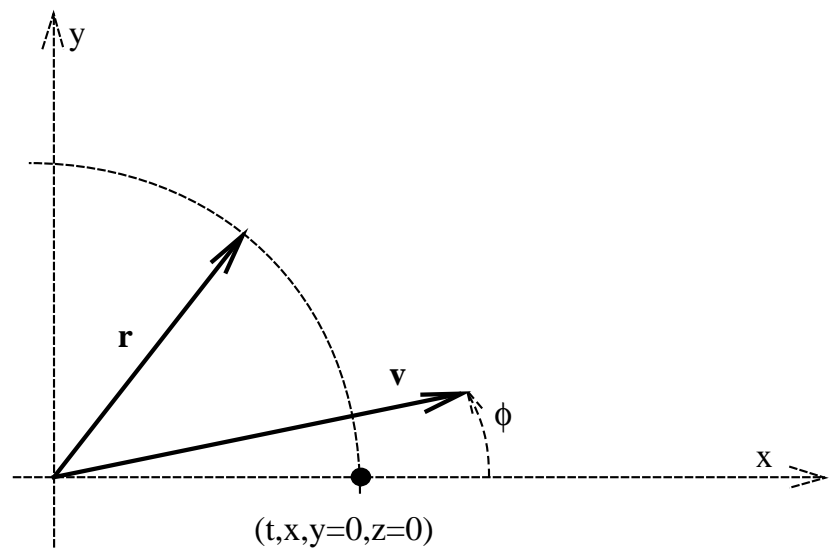


Figure 2.3: Cylindrical geometry of system. The z -axis (beam) is perpendicular to the plane of the figure.

for v_x , v_y , and v_z and evaluating the derivatives at $y = z = 0$:

$$\begin{aligned} \partial_t T^{00} + \partial_x T^{0x} + \partial_y T^{0y} + \partial_z T^{0z} &= \\ \partial_t T^{00} + \partial_x T^{0x} + \partial_y (wv\gamma^2 \frac{y}{x}) + \partial_z (w\gamma^2 \frac{z}{t}) &= \\ \partial_t T^{00} + \partial_x T^{0x} + \frac{1}{x} T^{0x} + \frac{1}{t} (T^{00} + P) &= 0, \end{aligned} \tag{2.2}$$

$$\begin{aligned} \partial_t T^{x0} + \partial_x T^{xx} + \partial_y T^{xy} + \partial_z T^{xz} &= \\ \partial_t T^{x0} + \partial_x T^{xx} + \partial_y (wv^2\gamma^2 \frac{y}{x}) + \partial_z (wv\gamma^2 \frac{z}{t}) &= \\ \partial_t T^{0x} + \partial_x T^{xx} + \frac{1}{x} (T^{xx} - P) + \frac{1}{t} (T^{0x}) &= 0. \end{aligned} \tag{2.3}$$

Rearranging and using the notation r instead of x , and keeping in mind $\tau = t$ for $z = 0$, we obtain

$$\begin{aligned} \partial_\tau (r\tau T^{00}) + \partial_r (r\tau T^{r0}) &= -rP, \\ \partial_\tau (r\tau T^{0r}) + \partial_r (r\tau T^{rr}) &= \tau P \end{aligned} \tag{2.4}$$

for the equations of motion at $z = 0$. It is from these equations that our cylindrically-symmetric Godunov algorithm is derived (see Section 2.4). The flows which are used to connect individual cells in this method are approximated by similarity solutions (see Section 2.5) and are derived from the one-dimensional equations of motion in t and x that are immediately evident from $\partial_\mu T^{\mu\nu} = 0$. Using one-dimensional similarity solutions is justified whenever there is no length or time scale to the problem, or when the size of the pattern is much smaller than the length scale of the problem. In our case, this means keeping the time step much smaller than the radial distance to a cell boundary.

2.2 Equation of State

Along with the geometry of the system, it is the equation of state (EOS) of the compressed matter that determines the evolution. The equation of state used for all our calculations has a first-order phase transition between a hadron phase, modeled as a non-interacting massless pion gas, and a quark-gluon plasma (QGP) modeled as a mixture of gluons and two flavors of massless quarks, u and d . In reality, there may be more flavors, but at the energies of

interest the u and d are the most abundant. More (massless) flavors could easily be added by increasing the number of degrees of freedom in the QGP phase. It will become apparent later in this section that for a gas of non-interacting massless particles, the various densities are proportional to the number of degrees of freedom, thereby simplifying the equation of state greatly. Since the pion is light on hadronic mass scales, the approximation of massless pions in the hadronic phase is quite physical. The bare masses of the u and d quarks are negligible compared to any mass or energy scale in our calculation. We assume that the baryon number is zero in the QGP phase, and (for most of the calculations) that the various species are in chemical equilibrium. Under these conditions the chemical potentials can be taken to be $\mu_i = 0$.

The equation of state for a massless pion gas can be calculated analytically. The energy density for a given temperature T is

$$e(T) = 3 \int \frac{d^3k}{(2\pi)^3} \frac{\epsilon(k)}{\exp[\epsilon(k)/T] - 1} , \quad (2.5)$$

where k is the momentum of a pion, $\epsilon(k)$ is the energy of a pion at momentum k , and the factor of 3 accounts for the 3-fold isospin degeneracy. For massless particles $\epsilon = k$, so we may write this as

$$e(T) = 3 \frac{4\pi}{(2\pi)^3} \int_0^\infty dk k^2 \frac{k}{\exp(k/T) - 1} . \quad (2.6)$$

The average pressure associated with a relativistic particle is 1/3 of its momentum k (for the three dimensions of coordinate space) times its velocity k/ϵ (proportional to the number of particles hitting a surface per unit time), so we may write the pressure of the hadron gas as

$$\begin{aligned} P(T) &= 3 \frac{4\pi}{(2\pi)^3} \int_0^\infty dk k^2 \frac{k/3}{\exp(k/T) - 1} \\ &= \frac{e(T)}{3} . \end{aligned} \quad (2.7)$$

The enthalpy density is $w = e + P = 4e/3$. The integrals can be evaluated [9] by using the binomial expansion, and contour integration to evaluate the resulting series, to give the well-known Stefan-Boltzmann results for black body radiation,

$$e(T) = c_h T^4, \quad (2.8)$$

$$P(T) = \frac{1}{3}c_h T^4,$$

$$w(T) = \frac{4}{3}c_h T^4,$$

where $c_h = 3\pi^2/30$ contains the pion degeneracy and the dimensionless part of the integral, and the subscript h stands for the hadron phase.

We assume massless quarks and gluons in the QGP, so we use a similar formula for the energy, and we add a vacuum energy density B :

$$e(T) = 16 \frac{4\pi}{(2\pi)^3} \int_0^\infty dk k^2 \frac{k}{\exp(k/T) - 1} \quad (2.9)$$

$$+ 24 \frac{4\pi}{(2\pi)^3} \int_0^\infty dk k^2 \frac{k}{\exp(k/T) + 1} + B$$

where the factor 16 comes from the spin (2) and color (8) degrees of freedom of the gluons, and the 24 comes from the 2 (flavors) \times 3 (colors) \times 2 (spins) \times 2 (q, \bar{q}) = 24 degrees of freedom from the massless u and d quarks and antiquarks which, in our model, are the only two flavors in the QGP. Evaluation of the second integral in (2.9) (see Appendix B.2) reveals that

$$\int_0^\infty dk k^2 \frac{k}{\exp(k/T) + 1} = \frac{7}{8} \int_0^\infty dk k^2 \frac{k}{\exp(k/T) - 1} \quad (2.10)$$

so each degree of freedom of a massless fermion can be thought of as 7/8 of an effective boson degree of freedom. The above formula is often written

$$e(T) = g_q \frac{4\pi}{(2\pi)^3} \int_0^\infty dk k^2 \frac{k}{\exp(k/T) - 1} + B \quad (2.11)$$

$$= c_q T^4 + B,$$

where $g_q = 16 + (7/8) \times 24 = 37$, and $c_q = g_q \pi^2/30$ and the subscript q stands for the quark phase.

The vacuum energy density B (“bag constant”) can be thought of as the energy that is needed to dissociate the quarks that make up hadrons, i.e. the latent heat of the hadron gas/QGP phase transition. The symbol B for the vacuum energy density originates in the MIT bag-model [10], but is used here in a more general sense and does not restrict the validity of the calculations to a specific model. We will see in a moment how the tendency

of the quarks to bind together, parametrized by B , reduces the pressure below what one would naïvely expect.

To find the expression for the pressure in the QGP phase, we take the expressions for the energy in the hadron and QGP phases and combine them with what we know about the entropy. Because the chemical potential $\mu = 0$, the entropy in the hadron phase is

$$s = \frac{e + P}{T} = \frac{4}{3}c_h T^3. \quad (2.12)$$

We assume that at a constant temperature T_c the entropy is proportional to the effective degrees of freedom. So the entropy at energy densities just below $e_q = c_q T_c^4 + B$ is

$$s_q = \frac{c_q}{c_h} s_h = \frac{4}{3}c_q T_c^3, \quad (2.13)$$

where s_h is the entropy at energy densities just above $e_h = c_h T_c^4$. We then use the Euler relations to find

$$P_c = s_q T_c - e_q = \frac{4}{3}c_q T_c^4 - (c_q T_c^4 + B) = \frac{1}{3}c_q T_c^4 - B \quad (2.14)$$

for the pressure at the phase transition. For $T > T_c$ the pressure must take the same mathematical form, so

$$P = \frac{1}{3}c_q T^4 - B. \quad (2.15)$$

As in the hadron phase, $w = e + P$, and because the fluid dynamics code works in terms of w and P (see section 2.6), it is useful to summarize the equation of state as follows:

$$T < T_c : \quad \begin{cases} w &= \frac{4}{3}c_h T^4, \\ P &= \frac{w}{4}, \end{cases} \quad (2.16)$$

$$T = T_c : \quad \begin{cases} w_h &\leq w \leq w_q, \\ \frac{w_h}{4} &= P = \frac{w_q}{4} - B, \end{cases}$$

$$T > T_c : \quad \begin{cases} w &= \frac{4}{3}c_q T^4, \\ P &= \frac{w}{4} - B, \end{cases}$$

where $w_h = (4c_h/3)T_c^4$ and $w_q = (4c_q/3)T_c^4$. Note that B is related to the transition temperature, T_c , by requiring equal pressures in the QGP and hadronic phases at $T = T_c$:

$$B = \frac{\pi^2(g_q - 3)}{90}T_c^4. \quad (2.17)$$

For QGP in chemical equilibrium we take $g_q = 37$. As pointed out in [7], immediately after the nuclei separate, the space between is occupied mostly by gluons, with the quark population reaching chemical equilibrium density only after several fermis. To simulate the scenario where the quark density may be less than equilibrium, we use $g_q = 16 + 21f$, where $0 \leq f \leq 1$. If B depends only on QCD properties, and not on any assumptions in our calculation, then T_c will increase with decreasing g_q (see Section 2.6). When we do the calculations with $f \neq 1$, the program calculates a B from the given T_c assuming equilibrium conditions ($g_q = 37$), and the resulting actual T_c is given by (2.17). It is useful to keep B the same for side by side comparisons of scenarios with and without chemical equilibrium. On all the figures in this work, the T_c label refers to the T_c given to the calculation, from which B is calculated.

The speed of sound in our model is $c_s = \sqrt{dP/de}$, which is true for any system wherein P depends only on e . In the hadron and QGP phases, this is $c_s = 1/\sqrt{3}$, and in the mixed ($T = T_c$) phase $c_s = 0$.

2.3 Estimating Initial Conditions

The isentropic expansion assumption allows us to use the entropy at the end of the collision, which we can estimate from the measured pion yield, to calculate the entropy density at thermalization time $\tau = \tau_0$, and thus the temperature T_0 at the beginning of the transverse expansion. Ideally, an experiment will measure the charged pion number per unit rapidity, dN_{ch}/dy , in the central-rapidity region. For the WA80 S+Au experiment, the experimenters estimated $dN_{ch}/dy = 150$ [3]. In the NA45 experiment, the experimenters estimated [4] the

closely related quantity $dN_{ch}/d\eta = 125$, where η is the pseudorapidity, defined as

$$\eta \equiv \frac{1}{2} \ln \left(\frac{1 + \cos \theta}{1 - \cos \theta} \right) = \frac{1}{2} \ln \left(\frac{p + p_z}{p - p_z} \right). \quad (2.18)$$

Rapidity, on the other hand, can be written as

$$y \equiv \operatorname{arctanh}(v_z) = \frac{1}{2} \ln \left(\frac{E + p_z}{E - p_z} \right). \quad (2.19)$$

One can see that for fastparticles, where $m \ll E$ and $p \simeq E$, $\eta \simeq y$. So the total (neutral+charged) pion rapidity densities for the WA80 and NA45 experiments are, by assuming isospin symmetry (π^+ , π^- , π^0), $dN_\pi/dy = 225$ and 188 respectively.

The entropy is directly related to the number of pions by the well known [2] fact that the entropy per massless boson is 3.6 (derived in Appendix B.1). Putting this together with the volume per unit rapidity in the Bjorken picture, $dV/dy = \pi R^2 \tau_0$, we have

$$s_0 = \frac{3.6 dN_\pi/dy}{\pi(1.2 \text{ fm})^2 A^{2/3} \tau_0}, \quad (2.20)$$

where A is the nucleon number of the smaller of the two colliding nuclei, and $r_0 = 1.2 \text{ fm}$ is the radius parameter in $R = r_0 A^{1/3}$, the formula which describes the radii of nuclei as a function of their nucleon number A .

2.4 The Godunov Method

This fluid dynamics code uses the Godunov method [11] to evolve Eqs. (2.4) in time. The Godunov method approximates the state of the system at the beginning of any given timestep as a collection of cells, each filled with matter of uniform density and velocity. At each intercell boundary we solve the problem whose initial conditions are two abutting semi-infinite regions; this provides the values of the flows an infinitesimal time after the profile between the two regions diffuses (Riemann solutions). The time-step is kept short enough that the flow patterns from opposite sides of the cell do not overlap. Then the conservation laws (2.4) are used (in the form of the Godunov equations, see (2.29) below) to calculate the new cell averages of T^{00} and T^{0r} . The changes in the cell averages can then be calculated at each timestep. In the case of one-dimensional flow, these changes can be expressed exactly because the flows are similarity solutions (discussed in Section 2.5) which

are time-independent at the cell wall. With cylindrical symmetry, similarity solutions are a good approximation as long as we choose the timestep small enough so that the rarefaction pattern is small compared to both the cell size and the characteristic length scale r .

Each of our cells is a cylindrical shell with inner radius r and outer radius $r + \delta r$, where δr is the cell size. The beginning and end of a timestep is given by τ and $\tau + \delta\tau$ respectively, where $\delta\tau$ is the timestep. In the derivation of the Godunov equations that follows, $-$ and $+$ designate the flows at the inner and outer edges of the cell, and the subscript 0 designates the value of a variable at the beginning of the timestep.

We use as an example the first equation of (2.4) and integrate it over a space-time cell. We integrate the first term over τ , obtaining

$$\int_{\tau}^{\tau+\delta\tau} d\tau \partial_{\tau}(r\tau T^{00}) = r \left[(\tau + \delta\tau)T^{00}(\tau + \delta\tau) - \tau T^{00}(\tau) \right]. \quad (2.21)$$

We then integrate over r to get

$$\begin{aligned} \int_r^{r+\delta r} dr r \left[(\tau + \delta\tau)T^{00}(\tau + \delta\tau) - \tau T^{00}(\tau) \right] = \\ \left[\int_r^{r+\delta r} dr r \right] \left[(\tau + \delta\tau)\Theta^{00}(\tau + \delta\tau) - \tau\Theta^{00}(\tau) \right], \end{aligned} \quad (2.22)$$

where we have defined the spatial average

$$\Theta^{\mu\nu}(\tau) \equiv \frac{\int_r^{r+\delta r} dr r T^{\mu\nu}(\tau)}{\int_r^{r+\delta r} dr r}. \quad (2.23)$$

It is the new values of $\Theta^{\mu\nu}$ that are computed for each cell, and describe the state of the system at each timestep in the Godunov scheme.

It is easier to integrate the second term in the opposite order:

$$\int_r^{r+\delta r} dr \partial_r(r\tau T^{0r}) = (r + \delta r)\tau T_+^{0r} - r\tau T_-^{0r}. \quad (2.24)$$

As mentioned earlier, we approximate the intercell flow with a similarity solution, which implies that T_+^{0r} and T_-^{0r} , the flows at the cell walls, are time-independent over the range

of integration. Thus the τ -integration is trivial:

$$\int_{\tau}^{\tau+\delta\tau} d\tau \left[(r + \delta r)\tau T_+^{0r} - r\tau T_-^{0r} \right] = \left[\int_{\tau}^{\tau+\delta\tau} d\tau \tau \right] \left[(r + \delta r)T_+^{0r} - rT_-^{0r} \right]. \quad (2.25)$$

Finally, we integrate the right-hand side, which involves the pressure P . This is somewhat more complicated than the other terms because one must make a couple of approximations. First, the r -integral of P is not known, except at the very beginning of the timestep when the matter is uniform. At the beginning of the timestep,

$$\int_r^{r+\delta r} dr (-rP) = - \left[\int_r^{r+\delta r} dr r \right] P_0, \quad (2.26)$$

where $P_0 = P(\Theta_0^{00}, \Theta_0^{0r})$ is the pressure calculated from the averaged tensor elements at the beginning of the timestep. Similarly, we can define the space-averaged pressure at the beginning of the next timestep to be $P_{new} = P(\Theta^{00}, \Theta^{0r})$, which would be the pressure associated with the uniform densities at that time. At this point, the values of Θ^{00} and Θ^{0r} are still unknown, so P_{new} is still unknown. However, one may reasonably make an approximation for the time average,

$$\int_{\tau}^{\tau+\delta\tau} d\tau \int_r^{r+\delta r} dr (-rP) = - \left[\int_{\tau}^{\tau+\delta\tau} d\tau \right] \left[\int_r^{r+\delta r} dr r \right] \frac{1}{2}(P_0 + P_{new}). \quad (2.27)$$

It turns out that with this approximation, the resulting expressions for the new Θ^{00} and Θ^{0r} are the same, to first order in $\delta\tau$, as those obtained by using the cruder assumption

$$\int_{\tau}^{\tau+\delta\tau} d\tau \int_r^{r+\delta r} dr (-rP) = - \left[\int_{\tau}^{\tau+\delta\tau} d\tau \right] \left[\int_r^{r+\delta r} dr r \right] P_0, \quad (2.28)$$

which involves only known quantities. This is shown in Appendix C.1.

In our calculation, we used P_0 to calculate an intermediate value of P , which was then used again to solve for the new values of $\Theta^{\mu\nu}$. The difference in the results in comparison to simply using P_0 was much smaller than that from other sources such as choice of timestep or cell size.

The second equation of motion in (2.4) is integrated much like the first. The results we

use are:

$$\begin{aligned}
 (\tau + \delta\tau)\Theta^{00} &= \tau\Theta_0^{00} - \frac{\delta\tau^2 + 2\tau\delta\tau}{\delta r^2 + 2r\delta r}[(r + \delta r)T_+^{0r} - rT_-^{0r}] + \delta\tau P_0, \\
 (\tau + \delta\tau)\Theta^{0r} &= \tau\Theta_0^{0r} - \frac{\delta\tau^2 + 2\tau\delta\tau}{\delta r^2 + 2r\delta r}[(r + \delta r)T_+^{rr} - rT_-^{rr}] + \frac{\delta\tau^2 + 2\tau\delta\tau}{\delta r + 2r}P_0.
 \end{aligned}
 \tag{2.29}$$

2.5 Similarity Solutions

As mentioned earlier, the flows between adjacent cells in the simulation are approximated by similarity solutions. Similarity solutions are patterns that develop in a system that has neither length nor time scales; the resulting pattern depends only on the variable $\chi = x/\tau$, where $x = 0$ is the junction between two semi-infinite regions and $\tau = 0$ is the moment when the regions are still uniform. At any given time τ , χ is proportional to the position x . Also, because of causality (information cannot travel faster than light), $\chi = \pm 1$ are the outermost limits of a similarity solution. Let us assume that at time $\tau = 0$, two one-dimensional semi-infinite uniform regions, each described by respective values of enthalpy density w and velocity v , abut each other at $\chi = 0$. A short time later a region will form around $\chi = 0$ which may be different than either of the two original regions. This joining region may be a combination of uniform regions, simple rarefaction waves and shocks. Because there is neither a length nor time scale, the w and v of the joining region (hereafter referred to as the “similarity pattern”) are functions of χ only. It turns out that there are nine different similarity solutions (combinations of uniform regions, rarefaction waves and shocks) to the two uniform cell problem, depending on the phase of matter in each cell. In each case the goal is to find the values of T^{0r} and T^{rr} at $\chi = 0$ so that Θ^{00} and Θ^{0r} may be computed for the next timestep.

In each of these similarity patterns, the number of degrees of freedom must match the number of constraints. In the system of counting used here, the only degrees of freedom are the values of w and v . One type of region that may form part of a flow pattern is a simple rarefaction wave, which only exists when the speed of sound c_s is finite, i.e. in a pure phase. If the values w_l and v_l are specified at its head, as in the common situation where the head meets and matches the left-hand cell, then there is one degree of freedom, the length, or equivalently, the value of v at the end of the rarefaction. The EOS of the fluid along with the differential equation that describes similarity rarefaction waves (see Appendix A.2)

completely determine the value of w at a given v , so the only degree of freedom is the value of v at which the rarefaction joins the next part of the flow pattern to the right, either a uniform region or the vacuum. It is possible to solve for the exact form of these rarefaction waves in the case of a constant speed of sound, e.g. an ideal massless relativistic gas; more generally, we may solve for the rarefaction wave numerically by integrating along χ . For a rarefaction wave, $\chi = (v \pm c_s)/(1 \pm vc_s)$, meaning that the pattern moves at the speed of sound c_s with respect to the fluid. Details of the calculation of both the rarefaction shape and the shock conditions are given in Appendix A. In the case where the values of w and v at the head are not specified, such as when the head is one side of a shock (a discontinuity), then the values of w and v at the head are counted as an additional two degrees of freedom. The other type of region that may form part of a flow pattern is a uniform region, which may exist in any phase of matter. A uniform region has two degrees of freedom, w and v , and the length is irrelevant as it is featureless.

The individual types of regions may be joined in a number of ways, which may carry constraints. The most trivial way is if w and v are both continuous across the joining ends of the two regions. An example of this would be either the case where a rarefaction's head is continuous with the dense matter it abuts, or the less dense end of a rarefaction may join a uniform region in a continuous manner. In my way of counting, there is no constraint, and we do not count the (w, v) pair as degrees of freedom in this case.

Another way two regions can be joined is with a shock discontinuity. For shocks there is a relationship that must be satisfied (see Appendix A.1) which provides one constraint:

$$\frac{[T^{0r}]}{[T^{00}]} = \frac{[T^{rr}]}{[T^{0r}]} = v_{sh}, \quad (2.30)$$

where $[T^{\mu\nu}]$ is shorthand for $T_L^{\mu\nu} - T_R^{\mu\nu}$. The tensor elements $T^{\mu\nu}$ depend only on the two quantities w and v , and v_{sh} is the velocity of the resulting shock. v_{sh} is not counted as a degree of freedom and the right-hand equality is not counted as a constraint; $\chi = v_{sh}$ is the location of the shock in the entire flow pattern.

The effect of this constraint is different depending on whether the shock joins regions of pure phase or mixed phase matter. In the case of pure phase matter, there is a set of solutions that satisfy the constraint. If one side of the shock is pre-specified as being described by (w_0, v_0) , then (w, v) , which describes the other side of the shock, must fall along a curve in (w, v) space. This is the one constraint. In the case of mixed phase matter,

where $c_s = 0$, it can be shown (see Appendix A.1) that v must be the same on both sides of the shock, and there is no constraint on the value of w , aside from being in the mixed phase. The one constraint here is only that v be continuous, and as a result of this, the shock moves at the velocity of the fluid.

Figure 2.4 illustrates how to match the degrees of freedom with the constraints. Starting at the left (the most negative χ) we have a uniform region of matter, which is the “left-hand” cell, having enthalpy density w_l , and velocity v_l . w_l is such that the fluid is in the QGP phase. This uniform region I is connected to a rarefaction wave, region II, by matching the values of both w and v at the head of the rarefaction to region I. The values of both w and v are determined for any χ along the rarefaction wave according to the differential equation that governs rarefaction wave similarity patterns (see Appendix A.2). At some value of χ , χ_{soln} , at the end of the rarefaction wave, the values of w and v solve the shock conditions for the the shock between uniform region III and the uniform region IV, the “right-hand” cell. A uniform region III extends from χ_{soln} out to the shock, whose position χ_{sh} is determined by the shock velocity v_{sh} , which in turn is determined by the values of w and v on the two sides of the shock. There is one degree of freedom that determines the state of uniform region III: the value of χ_{soln} . This is constrained by the condition required for a stable shock between regions III and IV, Eq. (2.30).

Another example is shown in Figure 2.5. On the left there is a uniform region of mixed phase matter that needs to be connected to the vacuum on the right. A shock, which carries one constraint, joins the mixed phase to the head of a rarefaction wave in the hadron phase. Because one side of the shock is part of a rarefaction wave, there is an additional constraint because for a rarefaction wave it is always true that $\chi = (v - c_s)/(1 - vc_s)$ (see Appendix A.2). If the pattern as a whole is to be constant with respect to χ , as it must be to be a similarity solution, then the speed v of any feature must match $\chi = x/\tau$. In this case, $\chi_{sh} = v_{sh}$. Therefore both degrees of freedom, w and v for the head of the rarefaction wave, are determined by the constraints introduced by requiring a stable shock and a stable similarity pattern for the flow. The right side of the rarefaction wave connects to the vacuum, and thus the velocity of the fluid at this end approaches the speed of light at $\chi = 1$.

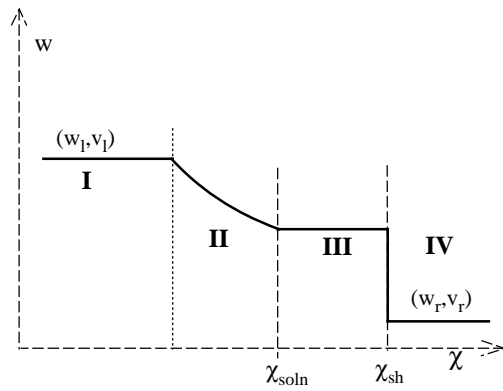


Figure 2.4: Joining two regions of pure phase matter.

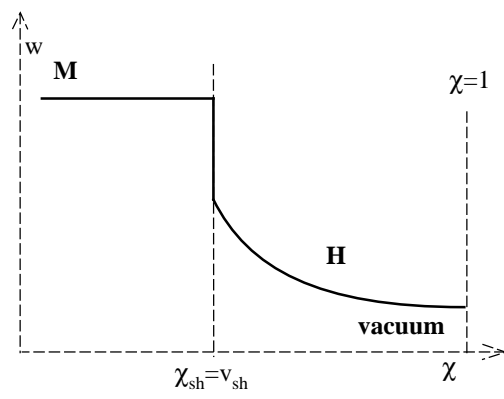


Figure 2.5: Joining a mixed phase region with the vacuum.

2.6 Fluid Dynamics Code

To implement the physics discussed above, I needed to write a relatively large (1500 lines) FORTRAN code, which is available at <http://cnr2.kent.edu/~neumann>. The main section of the program begins with input of the parameters which describe the overall picture of the collision: A , the nucleon number of the smaller nucleus; dN_π/dy , the total (charged plus neutral) pion multiplicity as measured at the end of the collision, which is used to provide an estimate of the initial temperature; τ_0 , the thermalization time of the fluid, and the time after maximum overlap when the transverse expansion begins; T_c , the transition temperature between a hadronic gas (modeled as a gas of massless pions) and the QGP (modeled as a gas of massless u and d quarks, and gluons); and a variable f , which provides a crude parametrization of non-equilibrium effects in the QGP ($f = 1$ corresponds to the equilibrium number of quarks, $f = 0$ no quarks; this is discussed in Sect. 2.2). All units are in MeV, fm, or combinations thereof. There are also two more inputs which provide control to the program. A varying timestep is used to exploit the fact that the most rapid changes happen near the beginning of the simulation, and so smaller timesteps are used there. Later in the simulation larger timesteps are adequate and are used to reduce computation. The timestep I used with good results was $\delta\tau = (\tau_0/tfact)(\tau/\tau_0)^{1/3}$; $tfact$ is the input parameter, and a value of 120 works well. As with other purely calculational parameters in the program, some experimenting was done to find values which gave results (usually measured from the resulting spectra) within 10^{-3} of a limiting value. Another input, $itrans$, is set to 1 or 0 to indicate whether or not to turn on the transverse expansion. All other parameters are “hard-wired” into the program, e.g. the radial cell size $\delta r = 0.1$ fm.

The outermost loop is the timestepping loop, which begins with $\tau = \tau_0$ and continues until $\tau = 80$ fm (300 fm if there is no transverse expansion). Approximately every 0.5 fm τ and (w, v) for each cell out to $r = 50$ fm are printed to the output. Inside the timestepping loop is the loop that goes through each radial cell from the innermost to the outermost ($r = 14R$, where R is the radius of the smaller nucleus). Cells beyond the outermost in the calculation are assumed to have $w = 0$ and $v = 1$. The goal at each cell is to calculate the change in Θ^{00} and Θ^{0r} , the respective spatial averages of T^{00} and T^{0r} . As described in Sect. 2.4, the changes depend only on the flows at the cell boundaries. For the innermost cell we use the boundary condition that there is no flow ($v = 0$) at $r = 0$, i.e. $T_-^{0r} = 0, T_-^{rr} = P$. At $r = \delta r$, the outer boundary of the cell, the program uses the subroutine *edgevalue* to

calculate the values of the flows T_+^{0r} and T_+^{rr} . Using these four flow values the changes in the Θ 's of the innermost cell are calculated using the Godunov equations. Then the program moves to the next cell out, making the old T_+^{0r} and T_+^{rr} the new T_-^{0r} and T_-^{rr} , and the flows T_+^{0r} and T_+^{rr} at the outer edge of this new cell are calculated using *edgevalue*. These new flows are used to calculate the changes in Θ^{00} and Θ^{0r} of that cell in turn, and so on moving outward until all the cells have been calculated, after which a new timestep begins.

2.6.1 Subroutine *edgevalue*

As may be surmised from the above description, the heart of the program is the subroutine *edgevalue*, which must do the work of finding the values of T_+^{0r} and T_+^{rr} at the next cell boundary. The description that follows is broken into several sections which describe what the code does to handle each combination of quark, hadron, or mixed phases. The beginning of the *edgevalue* subroutine tests for each possible case and branches to the appropriate type of similarity solution. In the following, w_l and v_l refer to the values of the enthalpy density and radial velocity in the radial cell whose changes are being calculated, and w_r and v_r refer to the values in the cell immediately outside this cell. This convention stems from my conceptualizing the situation as a one-dimensional similarity solution between left and right semi-infinite cells.

If the code finds that the two cells are identical ($w_l = w_r, v_l = v_r$), then we may take the values of T_+^{0r} and T_+^{rr} to be the same as those tensor elements measured in either cell. T^{00} , T^{0r} and T^{rr} are all computed from w and v with the subroutine *tmunu*.

In many cases, a uniform similarity solution will work to join two cells, although it is more difficult to find (w, v) that simultaneously satisfies the shock conditions with both (w_l, v_l) and (w_r, v_r) than it is to calculate a rarefaction/shock combination. Which method is used depends on which is easier in a given situation, and certain requirements stemming from matching the number of degrees of freedom with the number of constraints. Joining two regions of the same pure phase (quark or hadron gas) can always be accomplished using a rarefaction/shock combination (see Figure 2.6). Usually it is the case that $w_l > w_r$, but later in the evolution the opposite is sometimes true. To handle this case, the subroutine simulates the mirror-image situation by making the switch $w_r \rightarrow w_l, w_l \rightarrow w_r, -v_r \rightarrow v_l, -v_l \rightarrow v_r$, doing the calculation as usual, and then changing the sign of v at the boundary before returning the values of T^{0r} and T^{rr} .

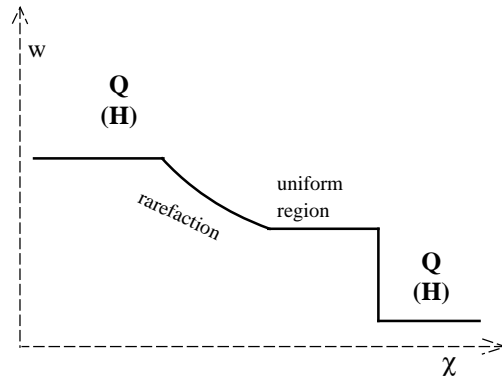


Figure 2.6: Cases 1 & 6: Joining regions of pure phase.

1. The code finds both w_l and w_r in the quark phase. The similarity solution that joins these is a rarefaction wave starting in the denser cell, connected to a uniform region and then a shock to the less dense cell. This solution is appropriate whenever two pure phase cells abut each other, as in the sixth case, hadron gas on both sides of the boundary.

As mentioned in Section 2.5 the goal is to find the values of T^{0r} and T^{rr} at the boundary between the cells, $\chi = 0$. The point $\chi = 0$ may fall in any of the four regions in the problem: if $v_l > c_s$ then a region described by (w_l, v_l) will cross $\chi = 0$; otherwise, either the simple rarefaction wave, the uniform region, or the right side (w_r, v_r) will cross it. The program searches along the rarefaction wave for $(w(\chi), v(\chi))$ which satisfies the shock conditions to join to the right-hand cell. The program solves for $w(\chi)$ numerically by taking small steps in rapidity $y = \text{arctanh}(v)$, (or equivalently, small steps in χ) changing w at each step according to the differential equation that describes the rarefaction wave. In the case where c_s is independent of w , w depends exponentially on y and can be found analytically. These analytic solutions are used to speed up the calculation in a specialized version of the program which I developed for the simple equation of state described in Section 2.2. First, χ for the head of the rarefaction wave is calculated; this is simply the relativistic difference of the fluid velocity v_l and sound speed c_s (which may be a function of w_l). The values of w_l and v_l at this χ provide a boundary condition for the equation which determines the shape of the rarefaction wave. This rarefaction wave extends to a value of $\chi = \chi_{soln}$ at which w and v satisfy the condition for a stable shock (derived in Appendix A.1). A uniform region described by this (w, v) extends from $\chi = \chi_{soln}$ to $\chi = v_{sh}$, where v_{sh} is the velocity of the shock joining the uniform region and the right-hand cell. If $\chi_{soln} > 0$ then the rarefaction wave crosses $\chi = 0$ and the values of w and v at that point can be found either analytically or by numerical integration from the head of the rarefaction wave to $\chi = \chi_{soln}$. If $\chi_{soln} < 0$ and $v_{sh} > 0$ then the uniform region crosses $\chi = 0$, and if $\chi_{soln} < 0$ and $v_{sh} < 0$ then we have (w_r, v_r) at $\chi = 0$. T^{0r} and T^{rr} are calculated with the subroutine *tmunu* and returned to the main program.

2. A cell of pure quark fluid abuts a cell in the mixed phase. The similarity solution that joins the cells is a uniform region consisting of one of the three phases (quark, mixed or hadron), depending on the relative velocities of the cells. Therefore connecting a

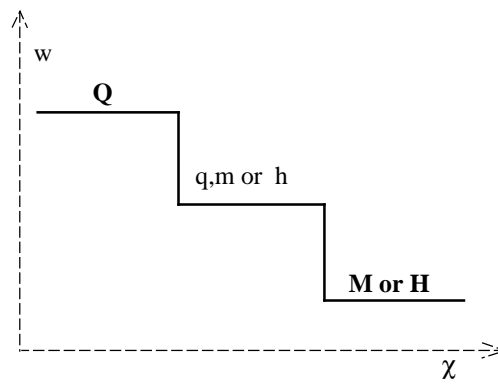


Figure 2.7: Cases 2 & 3: Joining quark phase matter with mixed phase matter.

region of quark matter “Q” and a region of mixed-phase matter “M” with a region of mixed-phase matter “m” is not too difficult computationally. Because of a certain constraint (see Appendix A.1) v of the connecting region “m” must match v_r of the mixed-phase matter “M”. w is varied within the mixed phase until (w, v) satisfies the shock condition with the matter on the left at (w_l, v_l) . If it is not possible to satisfy the shock condition with mixed-phase matter in the middle, then one must vary both w and v through other phases to satisfy the shock conditions between the joining region and the two cells. This is difficult enough that it was necessary to write a subroutine *t2shock* (see sect. 2.6.2) that specializes in searching for the (w, v) pair that makes the two shocks stable. Once a suitable (w, v) pair for the joining region is found, the resulting shock velocities are used to determine whether the left cell, joining region, or right cell cross $\chi = 0$ and the appropriate flows are calculated and returned to the main program.

3. A region of quark phase abuts the hadron phase. The two cells are connected with a uniform region as in case 2. Because the joining region can be any phase, it is necessary to use *t2shock* to solve for a suitable (w, v) .
4. There are two cells of mixed-phase matter. One can show (see Appendix A.1) that mixed-phase regions can only be joined by a shock, and that the shock conditions along with the vanishing speed of sound imply that the fluid velocity across the shock must be continuous, which removes a degree of freedom. Therefore, two cells of mixed-phase matter with arbitrary velocities cannot be joined with a uniform region of mixed-phase matter; the joining region must be either pure quark or pure hadron, depending on the relative velocities of the cells. Like the second and third cases, this is solved with subroutine *t2shock*.
5. A cell of mixed phase matter is connected by a uniform region of mixed or hadron matter to a region of pure hadronic matter. The values of w and v in the joining region are found with *t2shock*.
6. Pure hadron matter is in both cells. The solution is identical in form to the first case.
7. Quark phase matter is next to a vacuum. A rarefaction wave connects the quark phase on the left to the boundary between the mixed phase and quark phase w_Q , with the remaining pattern being that of mixed to vacuum, which is itself the eighth case.

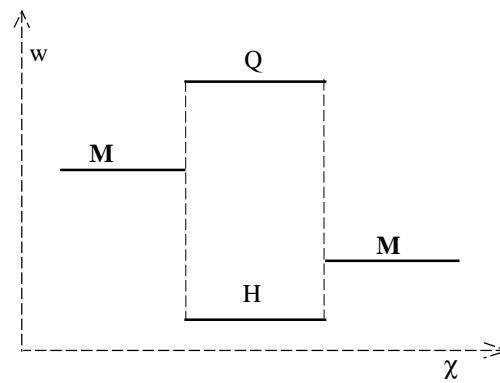


Figure 2.8: Case 4: Joining two mixed phase regions.

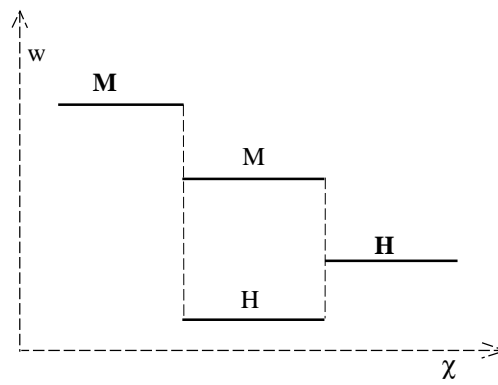


Figure 2.9: Case 5: Joining mixed phase matter with pure hadronic matter.

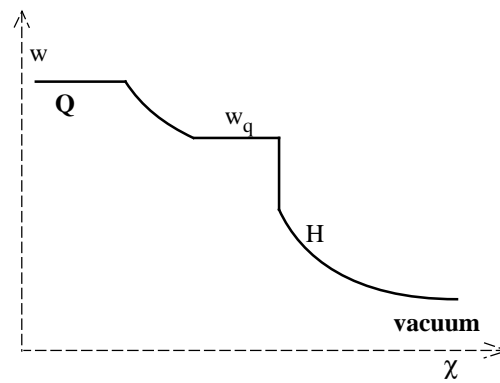


Figure 2.10: Case 7: Joining quark matter to the vacuum.

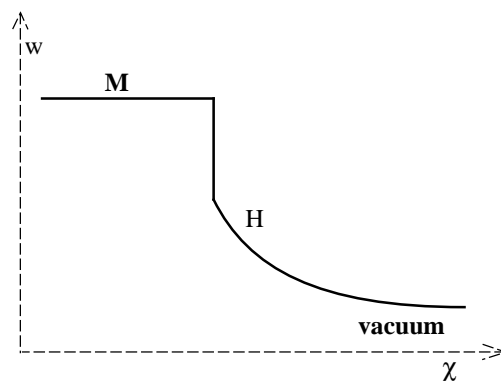


Figure 2.11: Case 8: Joining mixed phase matter to the vacuum.

8. The mixed phase matter is connected via a shock to a rarefaction wave comprised of hadronic matter, which extends smoothly to the vacuum at $\chi = 1$.
9. The case of hadronic matter to a vacuum is very similar, with the rarefaction wave starting with the left cell and extending smoothly to the vacuum.

2.6.2 Other Subroutines

There are several other functions of the program which deserve some description here. The subroutine *convert* solves for (w, v) given (T^{00}, T^{0r}) (this is the inverse function to subroutine *tmunu* which supplies T^{00}, T^{0r} , and T^{rr} given (w, v)). The previous value of (w, v) is also input to facilitate solution. Various first approximations to the solution are available to the program, for the cases when $v \approx 0$, $v \approx 1$ and $w \approx 0$. The first approximation is used as a starting point for a simple iterative solution which can accommodate any well-behaved equation of state.

The subroutine *t2shock* solves for (w, v) which simultaneously satisfies shock conditions on both the left and right. The input parameters are (w_l, v_l) , (w_r, v_r) , and an initial guess (w_0, v_0) . The initial guess is based on conditions evaluated in the calling routine *edgevalue*. *t2shock* uses an iterative 2-D Newton's method to simultaneously set two functions, σ_1 and σ_2 , to zero. These functions are measures of how well the (w, v) values in the joining region satisfy the shock conditions on either the left or right, and are defined as

$$\sigma_1 = [T^{00}]_L [T^{rr}]_L - [T^{0r}]_L^2, \quad (2.31)$$

$$\sigma_2 = [T^{00}]_R [T^{rr}]_R - [T^{0r}]_R^2,$$

where the L and R subscripts refer shocks between the joining region and the left and right cells. Sections of code are provided to break out of the normal search pattern if the search happens to wander into a region of (w, v) space where Newton's method does not approach the solution. If the solution is still not found in some finite number of iterations, then an error flag is returned to the calling routine which then tries another initial guess (w_0, v_0) . This happens rarely, and *edgevalue* has provisions to make an educated guess, much like the methods used by others [12] of what the inter-cell flows should be. Finally, the solution (w, v) is used to calculate the velocities of the shocks and then all these values are returned to the calling routine.

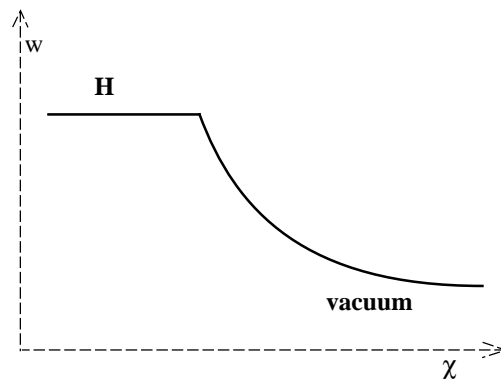


Figure 2.12: Case 9: Joining hadronic matter to the vacuum.

The rest of the program is made up of subroutines that do elementary and well-known jobs such as calculating partial derivatives, measuring errors, solving the Godunov equations, supplying the equation of state, and printing out the results.

2.7 Fluid Dynamics Results

This section contains illustrative results of the fluid dynamics calculations. The output of the hydro code is piped into a program that takes the discretized data and searches between space-time cells for surfaces of constant enthalpy density or radial velocity. This is done with a simple interpolation between neighboring cells or timesteps, and pairs of coordinates are sent to a file, which is plotted. No attempt is made to connect the points into lines, as they are close enough together to allow grouping by visual inspection.

Here we display results for S+Au collisions with $dN/dy = 225$, and $T_c = 150, 170$, and 200 MeV for the standard parameter set, and variations in τ_0 and f , the QGP equilibrium parameter. The thick lines (actually the “lines” formed by the larger dots) represent lines of constant enthalpy w during the evolution of the collision. The thinner lines are lines of constant radial velocity v . These will be referred to as “iso- w ” and “iso- v ” lines.

In Figure 2.13, one can see from the inside of the cylinder ($r = 0$) out, iso- w lines corresponding to w_q , the QGP side of the phase transition, w_h , the hadron side of the transition, and then an iso- w for w_{fo} , the freeze-out enthalpy density. The iso- v lines, from the inside out, correspond to $v = 0.01, 0.1, 0.4, 0.6, 0.7, 0.8$ and 0.9 . On an ultrarelativistic scale, we can think of $v = 0.01$ as being zero for practical purposes. The edge of the cylinder at $\tau = 0$ is at about 3.7 fm, and the expansion of the fluid is shown by the fanning of the lines away from this point. The line (in the lower right-hand corner) extending from the same point with a slope corresponding to the velocity of light is an artifact of the plotting procedure and should be ignored. The $v = 0.9$ iso- v line can be seen to extend nearly straight out from the initial edge of the cylinder; this signifies the outermost fluid being accelerated to a high velocity and then continuing outward undisturbed until much later when it is accelerated by the fluid further inside.

Moving inward, we can follow the rarefaction signal path by seeing where the fluid velocity starts to increase above zero. The $v = 0.01$ iso- v line, starting from $\tau = 0, r = 3.8$ fm, shows neatly that the information about the expansion on the outside flows inward at a constant rate about equal to the speed of sound in the QGP, $c_s = 1/\sqrt{3}$. The area on the

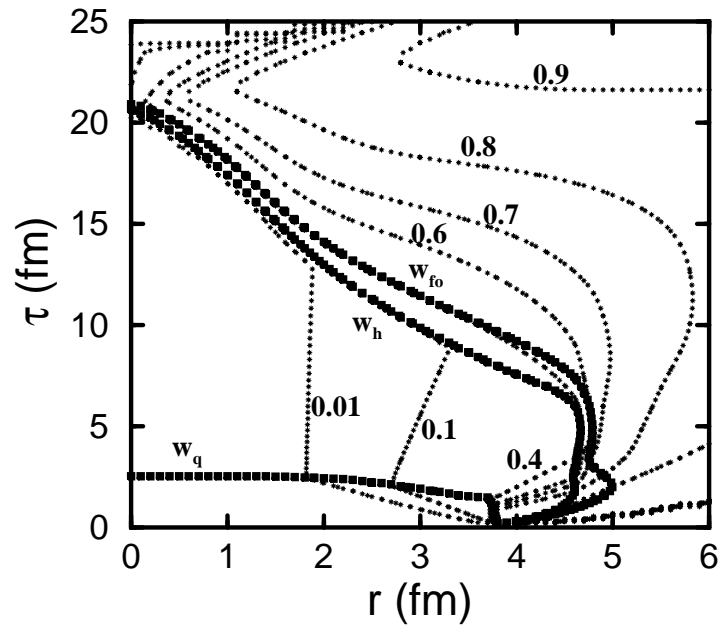


Figure 2.13: Profiles of w and v for S+Au, with standard set, $dN/dy = 225$, and $T_c = 150$ MeV.

diagram enclosed by $w_h < w < w_q$ is the mixed phase. The pressure in the mixed phase is a constant, P_c , and so there is no pressure gradient in the fluid to cause acceleration. This manifests itself in the diagram as a number of straight iso- v lines, whose slopes correspond to the values of v ; the same slopes are seen in all the figures.

Moving forward in time from the mixed phase, the iso- v lines slope inward again as the pressure gradient of the hadron gas causes more expansion. The freeze-out iso- w line, which for the standard set of parameters corresponds to $T = 120$ MeV, is close to the $w = w_h$ line, and they both reach the center of the cylinder around $\tau = 21$ fm. By this time, all of the fluid is moving outward, and the density is low enough that the weak pressure gradients cause very little acceleration; the iso- v lines extend almost straight out from this region of the diagram, indicating the fluid is moving freely outward, much like in the mixed phase.

It is worth noting the effect of raising T_c (see Figs. 2.14 & 2.15). As expected, the $w = w_h$ line moves away from the freeze-out line, which is a constant $T = 120$ MeV. A more interesting feature is that for a greater temperature difference $T_c - T_{fo}$, there is more transverse expansion by the time matter in the system reaches T_{fo} . This has a large effect on the e^+e^- spectra, and is responsible for a correlation between T_c and T_{fit} when freeze-out dominates (see Section 4.6). For the standard set, with $T_c = 150$ MeV the fluid velocity at freeze-out is close to $0.4 c$, with $T_c = 170$ MeV, $v \sim 0.5$, and with $T_c = 200$ MeV, $v \sim 0.6 - 0.7$. It is also interesting that for most of the mixed phase matter, $v < 0.1$; almost all the fast-moving matter is hadronic gas.

The graph for $\tau_0 = 1$ fm (see Fig. 2.16) looks surprisingly similar to that for the standard set (with $\tau_0 = 0.2$ fm). This is primarily because the temperature at the long thermalization time $\tau_0 = 1$ fm is very close (because there is little transverse expansion by this time) to what it is at $\tau = 1$ fm in the calculation with $\tau_0 = 0.2$ fm. In the limit where there is no transverse expansion, i.e. the Bjorken picture [5, 32], the fluid-dynamical evolution after τ_0 is independent of τ_0 . In the $\tau_0 = 0.2$ fm case, the transverse fluid motion up until $\tau = 1$ fm has a small effect: comparing Figs. 2.13 and 2.16 reveals that there is some increase in the 4-volume of the mixed phase with larger τ_0 , and this increases particle production, particularly in the case of photons [13] (see Sect. 3.3). Inspection of the iso- v lines in the mixed phase also shows that there is less outward fluid motion, which reduces the apparent temperature of the particles produced in the mixed phase.

For $f = 0.7$, we expect the QGP phase to be hotter at τ_0 to achieve the same initial entropy density as with $f = 1$. This results in a slightly faster expansion before the hadronic

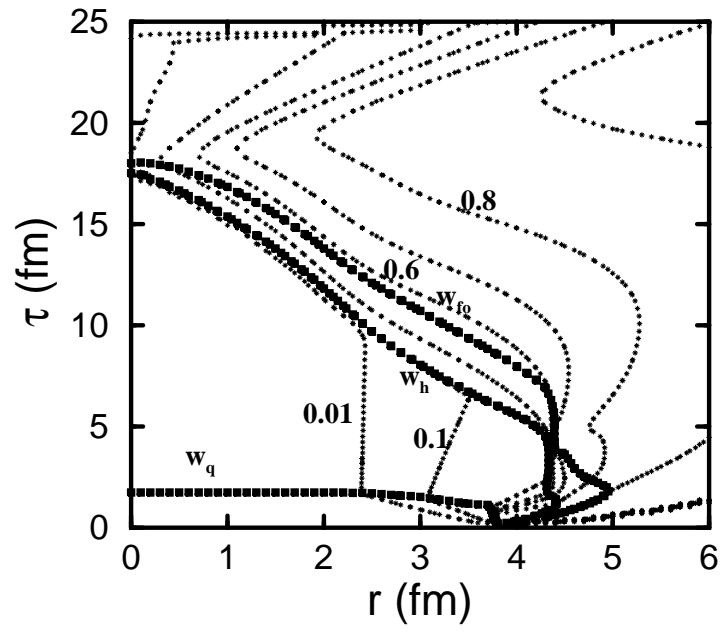


Figure 2.14: Same as Fig. 2.13, with $T_c = 170$ MeV.

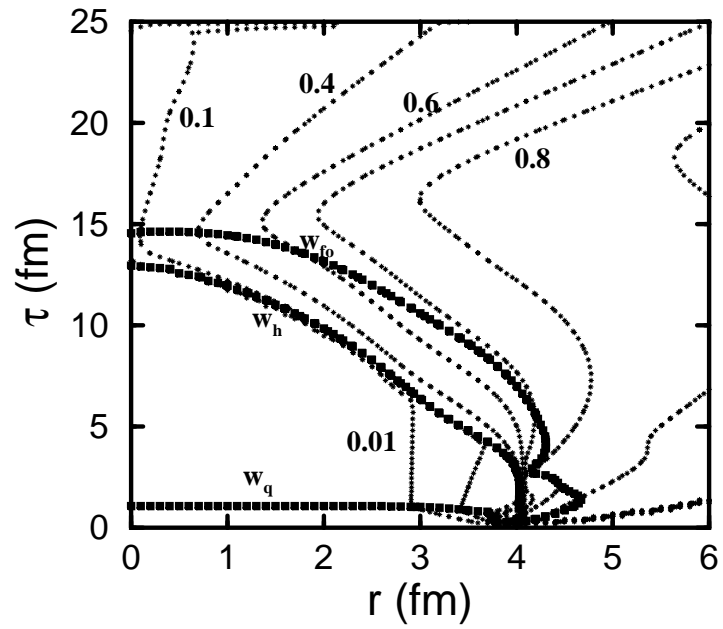


Figure 2.15: Same as Fig. 2.13, with $T_c = 200$ MeV.

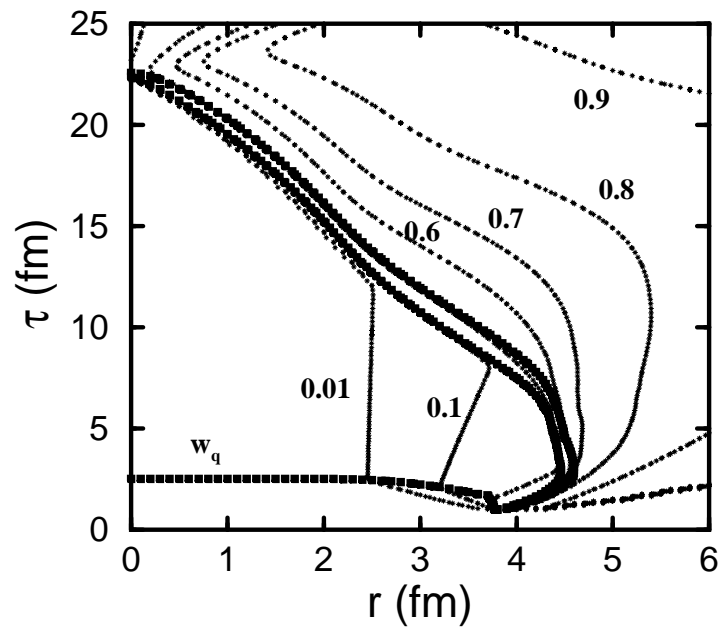


Figure 2.16: Profiles for $\tau_0 = 1$ fm, $T_c = 150$ MeV.

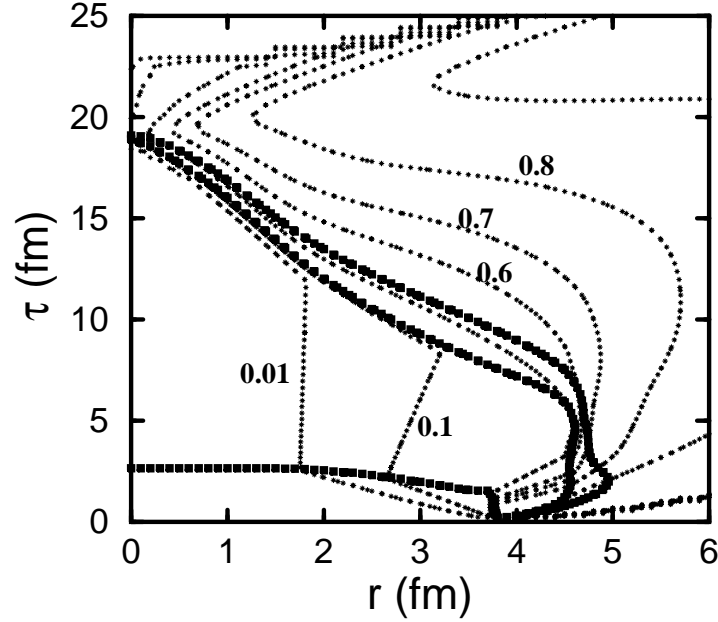


Figure 2.17: Profiles for $f = 0.7$, $T_c = 150$ MeV.

phase is reached (compare Figs. 2.13 and 2.17).

A profile of a Pb+Pb collision is shown in Fig. 2.18. The larger nuclear size results in a longer overall evolution, and more mixed phase matter. As will be seen in Sects. 3.3 and 4.6, this results in a much larger particle production cross section. A S+Au collision with $dN/dy = 188$ is shown in Figure 2.19. It is almost the same as the collision shown in Fig. 2.13, but the lower initial entropy density leads to reaching the hadronic phase sooner.

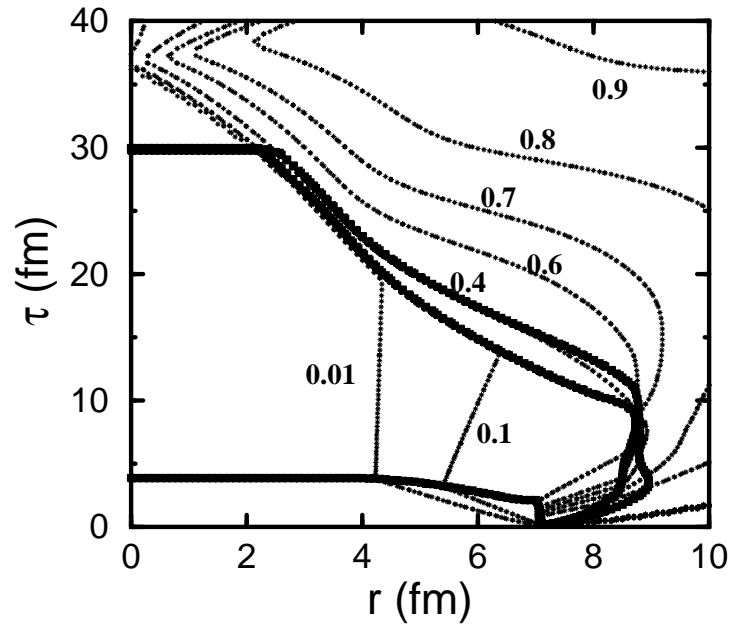


Figure 2.18: Profiles for Pb+Pb ($dN/dy = 1200$) and $T_c = 150$ MeV.

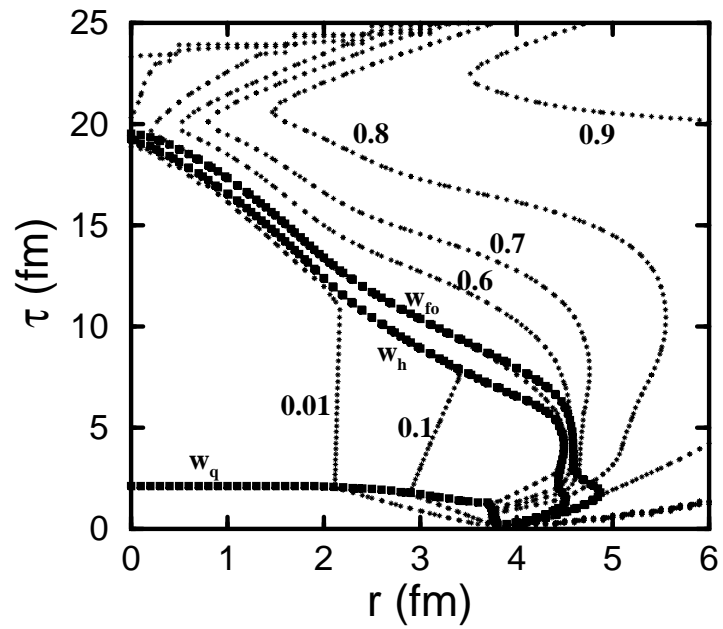


Figure 2.19: Profiles for S+Au with $dN/dy = 188$ and $T_c = 150$ MeV.

Chapter 3

Photon Production

In Chapter 2 we showed how local temperature and velocity can be calculated for a collision, using a simple fluid dynamical model that incorporates transverse expansion. In this chapter I explain how we use that information to calculate single photon spectra in the transverse momentum range $1 \leq p_T \leq 2$ GeV [13]. The choice of this window reflects the applicable range of the rate formula [14] when the transverse velocity boost due to the fluid motion is taken into account. This overlaps to a large degree the fitting windows used by the WA80 experimenters as well [3].

3.1 Space-Time Evolution of Photon Production

The photon production is calculated over the entire history of the collision after $\tau = \tau_0$. The integral for all photons produced is set up as follows: We must integrate over all fluid rapidities $y_f = \text{arctanh}(z/t)$, where z is the distance along the beam axis and t is the time measured in the center of mass (CM) frame. We also integrate over all proper times after $\tau = \tau_0$ (measured in each rapidity slice dy_f), the entire volume of the hot matter in the slice dy_f , and all possible momenta of a photon (which we measure in the rest frame of the fluid). The production rate dR/d^3p is a function of the temperature, viewed in the rest frame of the fluid. Let N be the total number of photons, produced anywhere in the fluid, and having any momentum. We may write

$$N = \int_{-\infty}^{\infty} dy_f \int_{\tau_0}^{\infty} d\tau \int_0^{\infty} 2\pi r dr \int_0^{\pi} d\phi \int_{-1}^1 d(\cos \theta) \int_0^{\infty} dp p^2 \frac{dR}{d^3p}. \quad (3.1)$$

Note that we have written the volume element of the cylinder as $d^3r = 2\pi r dr \tau dy_f$ by assuming boost invariance. ϕ and θ are the azimuthal and polar angles respectively, *viewed in the rest frame of the fluid*, of a photon.

We may select photons at $y = 0$ (central rapidity) and at a given transverse momentum p_T by inserting delta functions into the integral for N :

$$\begin{aligned} \frac{d^2N}{p_T dp_T dy} \Big|_{y=0} &= \int_{-\infty}^{\infty} dy_f \int_{\tau_0}^{\infty} d\tau \int_0^{\infty} dr 2\pi r \int_0^{\pi} d\phi \int_{-1}^1 d(\cos\theta) \\ &\times \int_0^{\infty} dp p^2 \frac{dR}{d^3p} \delta\left(\frac{1}{2}p_T^2 - \frac{1}{2}p_T'^2\right) \delta\left[y_f - \frac{1}{2} \ln\left(\frac{1+\cos\theta}{1-\cos\theta}\right)\right]. \end{aligned} \quad (3.2)$$

Note that the integral over y_f is trivial as nothing further inside the integral depends on it. The argument of the p delta function is $\frac{1}{2}p_T^2 - \frac{1}{2}p_T'^2$ rather than $p_T - p_T'$ because we want $p_T dp_T$ rather than just dp_T on the bottom of the differential cross section. For the integral over p we need to know the value of p (the fluid frame photon momentum) which gives the desired transverse momentum p_T' (as measured in the CM frame of the collision).

We write p_T' , the transverse momentum viewed in the CM frame, as a function of the photon momentum p_* , and the angles ϕ , and θ , all viewed in the fluid rest frame:

$$p_T'^2 = p_*^2 \gamma^2 \left[\sin^2\theta + 2v \sin\theta \cos\phi + v^2 (1 - \sin^2\theta \sin^2\phi) \right]. \quad (3.3)$$

This may be easily inverted to give p_* in terms of $p_T'^2$. After eliminating the y_f and p integrals with the delta functions we are left with

$$\frac{d^2N}{p_T dp_T dy} = \int_{\tau_0}^{\infty} d\tau \int_0^{\infty} dr 2\pi r \int_{-1}^1 d(\cos\theta) \int_0^{2\pi} d\phi \left(\frac{p_*^3}{p_T^2} \frac{dR}{d^3p} \right)_{p=p_*}. \quad (3.4)$$

Eq. (3.4) leaves out photon production before τ_0 . We estimated this assuming constant temperature T_0 from $\tau = 0$, defined as the time of maximum overlap of the nuclei, until τ_0 and we found this contribution negligible, less than 10^{-3} of the total due to (3.4). It should also be mentioned that we set $dR/d^3p = 0$ when $T < T_{fo}$, where T_{fo} is the ‘‘freeze-out’’ temperature, under which thermal equilibrium is assumed not to take place because of the long mean-free paths.

The evaluation of Eq. (3.4) results in nearly-exponential spectra. We then mimic the experimental procedure and extract a temperature (the fit temperature, T_{fit}) from the

obtained spectra. For fitting purposes, we take (3.4) without the time integration and with $v = 0$ in order to simulate the instantaneous spectrum of photons coming from fluid without transverse expansion, as in the Bjorken picture (see Chapter 2). This results in the formula [15]

$$\frac{d^2 N}{p_T dp_T dy} \sim \frac{T^{5/2}}{p_T^{1/2}} e^{-p_T/T} \ln \left(\frac{2.912 p_T}{g^2 T} + 1.12 \right), \quad (3.5)$$

which is accurate to about one percent for the range of p_T that we consider here. The amount of transverse expansion varies throughout a collision, so using a pure Bjorken expansion to fit a temperature provides an unambiguous standard for comparison.

3.2 Photon Production Rates

The photon production rate from thermally and chemically equilibrated quark-gluon plasma is, to first order in α_s , [14]

$$\frac{dR}{d^3 p} = \frac{5 \alpha \alpha_s}{18 \pi^2 p} T^2 e^{-p/T} \ln \left(\frac{2.912 p}{g^2 T} + 1 \right), \quad (3.6)$$

where $\alpha = 1/137$, and $\alpha_s = g^2/4\pi = 0.4$. (we use the semi-empirical formula of Ref. [14], which is almost identical to the exact rate). The value of the strong coupling constant α_s at the temperatures considered in this work is not well known, but a value $\alpha_s = 0.4$ is consistent with a comparison between perturbation theory and lattice gauge simulations [14, 16].

We also use Eq. (3.6) for the hadron gas, as its uncertainty is larger than the difference between the first-order QGP and hadron gas production rates, as calculated in [17]. The formula given by Nadeau, Kapusta and Lichard describes photons produced by the collisions of hadrons that inhabit the low-temperature phase.

The contribution of the a_1 resonance in the reaction $\pi\rho \rightarrow a_1 \rightarrow \rho\gamma$ was discussed recently by several authors [18, 19, 20] and found to be significant. The contribution of the a_1 meson can be parametrized as [18]:

$$\frac{dR}{d^3 p} = 2.4 \frac{T^{2.15}}{p} \exp \left(\left[-(1.35 p T)^{-0.77} - p/T \right] \right) (\text{fm}^{-4} \text{GeV}^{-2}). \quad (3.7)$$

We add this (neglecting interference effects) to the rate given by Eq. (3.6) to obtain our total photon production from the hadron gas.

3.3 Results

Some typical photon spectra are shown in Figure 3.1 for calculated 200 GeV/nucleon S+Au collisions, such as those measured in the WA80 [3] experiment. No cuts were applied, as the WA80 experimenters only used a cut in pseudorapidity, which falls well outside the midrapidity area we are calculating. We have used for our “standard” calculation $\tau_0=0.2$ fm/ c , $f=1$, and freeze-out temperature $T_{fo} = 120$ MeV. We have also included the a_1 resonance in the standard scenario. The initial entropy density was estimated from the experimentally measured value $dN_{ch}/dy = 150$ [3]. If a different value of one of the parameters is given, it is to be assumed that the others are held at the standard values.

Fig. 3.1 displays the effect on the spectra of varying the parameters, keeping the value of the critical temperature fixed ($T_c = 170$ MeV). We plot $d^2N_\gamma/p_T dp_T dy$ vs. p_T for different scenarios, and the calculated spectra are found to be nearly exponential. It is seen that increasing the equilibration time (i.e. decreasing the initial temperature) decreases the high p_T contribution to the photon spectrum and thus decreases the fit temperature. Increasing the freeze-out temperature from 120 MeV to 150 MeV removes a fraction of the radiated photons and decreases the yield, also as expected. Excluding the a_1 resonance decreases the yield by about one-third in the transverse-momentum range investigated. This is roughly consistent with several other calculations [18, 19, 20, 21].

In Fig. 3.2, we vary T_c from 150 to 200 MeV and calculate the resulting values of the temperature, T_{fit} , needed in Eq. (3.5) to fit the resulting spectrum for a central S+Au collision at SPS energy. Our standard value for the equilibration time, $\tau_0=0.2$ fm/ c , implies an initial temperature of $T_0 = 348$ MeV for the S+Au system.

In the absence of transverse expansion, T_{fit} is a monotonically increasing function of T_c , so one can infer T_c given T_{fit} from the measured photon spectrum [15]. This can be seen in the lowest curve, where we have run our simulation without transverse expansion.

Including transverse expansion, we find that we can no longer infer T_c from T_{fit} , due to the non-monotonicity of the relation (except for long thermalization times; see the curve with $\tau_0=1.0$ fm/ c , corresponding to $T_0 = 203$ MeV). This demonstrates the large effect of the transverse motion of the fluid on the photon spectrum: lowering T_c decreases the bag

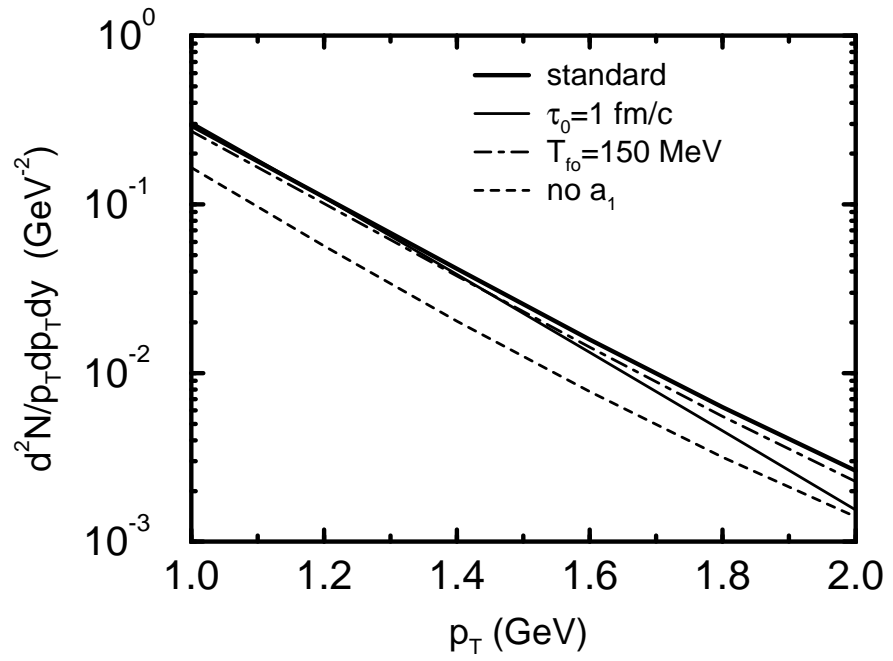


Figure 3.1: Photon spectra in a central S+Au collision at SPS energy with different parameter sets and $T_c = 170$ MeV. The standard set has $\tau_0 = 0.2$ fm/c, $f=1$, and $T_{fo} = 120$ MeV. The other sets differ from the standard one in the value of the parameter indicated.

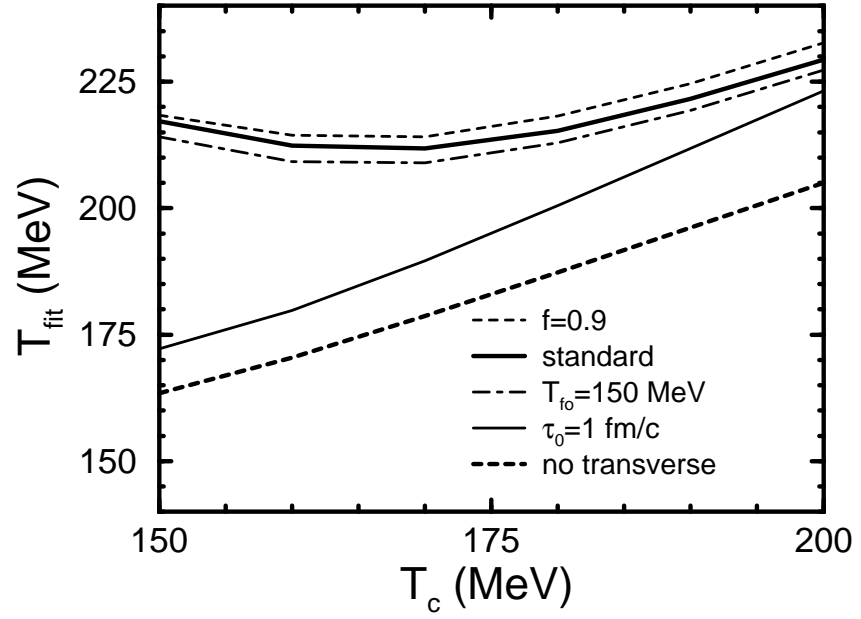


Figure 3.2: T_{fit} vs. T_c for photons in a central S+Au collisions at SPS energy with various parameter sets.

constant, which increases the ratio P/e in the QGP, producing more transverse motion. The increase in p_T caused by the fluid motion is enough to overcome the decrease of T_{fit} with decreasing T_c found without transverse expansion. This non-monotonicity occurred for all parameter sets we tried, although for some (e.g., $\tau_0 = 1$ fm/c) the minimum appears outside the range of T_c investigated here. As the initial temperature is lowered, the value of T_c below which the effects of flow dominate also decreases. This may be attributed to the fact that, as T_0 approaches T_c , less flow develops before the mixed phase is reached.

Contrary to experience without transverse expansion [15], increasing T_{fo} to 150 MeV decreases T_{fit} , another indication that the transverse motion has a large effect on the spectrum. Apparently the lower-temperature hadronic matter expands outward at a velocity high enough that the contribution to p_T from this motion more than makes up for the low temperature. Thus, removing the contribution from the late stages (by raising T_{fo}) decreases T_{fit} .

For $f \neq 1$, the quantity we call T_c on the figure is the chemical equilibrium ($f = 1$) transition temperature,

$$T_c = \left(\frac{90}{34\pi^2} B \right)^{1/4}, \quad (3.8)$$

rather than the larger non-equilibrium transition temperature used in the simulation, discussed in Sect. 2.2. We do this because the equilibrium transition temperature is more useful for comparisons with theoretical calculations. The curve for $f = 0.9$ shows that T_{fit} is about 3 MeV higher than for $f = 1$. The increase occurs because the temperature of the mixed phase, which makes a large contribution to the photon spectrum, is raised when f is lowered. We do not show results for other values of f ; the change in T_{fit} is approximately linear in f .

The effect of increasing τ_0 to 1 fm/c is dramatic: T_{fit} becomes monotonic within the range of interest, and is lower than for the other parameter sets considered. As mentioned above, this is due to the decrease in the role of the transverse expansion, which is assumed to start at τ_0 .

Figure 3.3 shows $d^2N_\gamma/p_T dp_T dy$ vs. p_T (per central collision) for the preliminary WA80 data (assuming a minimum bias cross-section of 3600 mb), along with calculated spectra using selected parameter sets. The data between 1 and 2 GeV are best fitted with $T_{fit} = 213$ MeV, using Eq. (3.5). We use this value of T_{fit} and Figure 3.2 to extract the value of T_c (between 150 and 200 MeV) for each parameter set. The experimentally determined fit

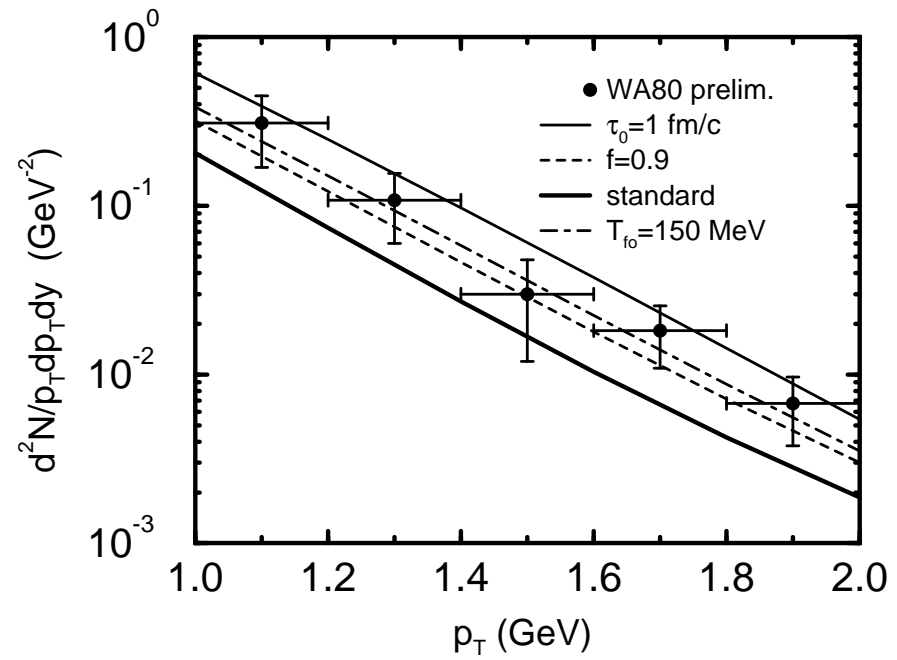


Figure 3.3: Preliminary WA80 data and selected fits. For each curve the value of T_c giving $T_{fit} = 213$ MeV from Fig. 3.2 is used as explained in the text.

temperature, $T_{fit} = 213$ MeV is below the values predicted by the model for some parameter choices. In these cases T_c was estimated by minimizing T_{fit} .

For the standard parameter set we used $T_c=160$ MeV. Note, however, that values of $160 \text{ MeV} \leq T_c \leq 170 \text{ MeV}$ all give very similar fits to the data. The total photon yield is larger for a higher value of T_c due to the large contribution from the mixed phase. Thus, even if T_c cannot be determined by T_{fit} alone, it may be possible to ascertain T_c by comparing to the total photon yield as well.

$T_c=170$ MeV is used for $f = 0.9$, but one should keep in mind the non-equilibrium transition temperature is larger than this, as explained earlier (Eq. 3.8). The difference is sufficient to counteract the decrease in the number of degrees of freedom in the plasma, leading to a somewhat higher yield than with the standard parameters. Due to the large error bars of the preliminary WA80 data, the calculated spectra are consistent with the data points, although generally below them for these parameters. In the absence of transverse expansion, photon production is increased by approximately a factor of two by including pion masses [15], so agreement with the preliminary WA80 data will probably be further improved with a more realistic equation of state.

Increasing the equilibration time to $\tau_0=1$ fm/ c (and accordingly decreasing the initial temperature) leads to $T_c=190$ MeV. The increase in T_c increases the photon yield. In addition, the lower initial temperature and the higher critical temperature results in less flow being built up by the time the system reaches the mixed phase than with the standard parameter set. Therefore, the system spends a longer time in the mixed phase for this set of parameters. This also increases the yield, as pointed out by Shuryak and Xiong [21]. To quantify the difference between these scenarios, we “measured” (in the code) the total four-volume associated with the mixed phase and found it to be about 25% larger for $\tau_0=1$ fm/ c than for $\tau_0=0.2$ fm/ c . Our results with the long equilibration time ($\tau_0=1$ fm/ c) tend to overestimate the data. Excess photons come from both the QGP and the hadronic phases in our calculation relative to Ref. [21].

Increasing the freeze-out temperature to $T_{fo}=150$ MeV decreases the photon yield because a contribution is removed, which more than makes up for the fact that we used $T_c = 180$ MeV (rather than 160 MeV) in this case. Note that $160 \text{ MeV} \leq T_c \leq 170 \text{ MeV}$ all give approximately the same T_{fit} for $T_{fo}=150$ MeV, though the photon spectrum has a larger magnitude when T_c is increased due to the large contribution from the mixed phase. Thus, even if T_c cannot be determined by T_{fit} alone, it may be possible to ascertain T_c by

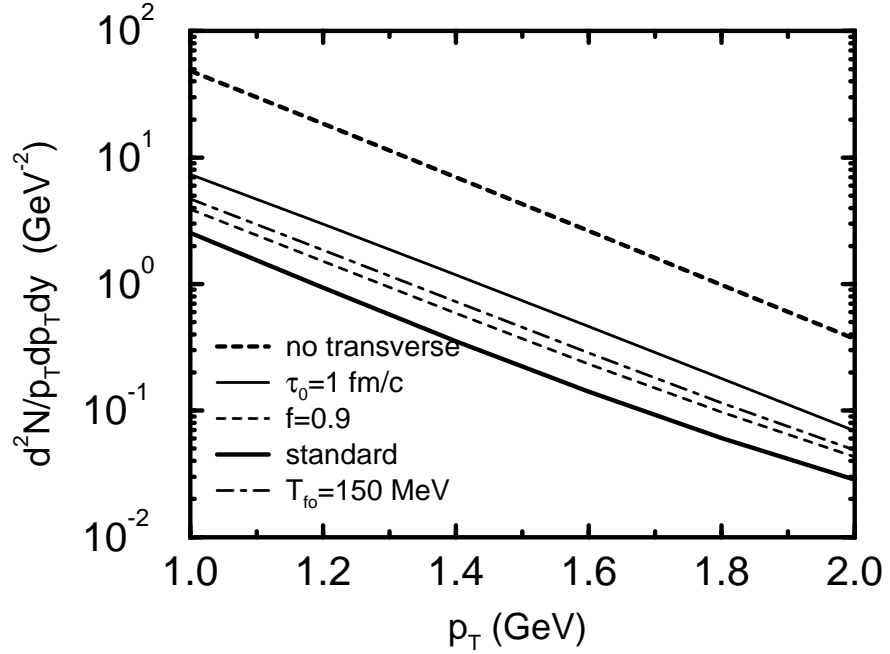


Figure 3.4: Predicted photon spectra for central Pb+Pb collisions at SPS energy.

comparing to the total production rate as well.

Figure 3.4 displays predicted spectra for a central Pb+Pb collision at SPS energy, using the parameter sets from Fig. 3.4. The initial temperatures corresponding to $\tau_0 = 0.2$ fm/ c and $\tau_0 = 1$ fm/ c are $T_0 = 432$ MeV and $T_0 = 252$ MeV, respectively. The shapes of the spectra and the relative production rates are similar to those for the S+Au collisions. For comparison, we also show the spectrum obtained in the absence of transverse expansion, taking $T_c = 200$ MeV. We find that transverse expansion has a large effect on the production rate.

The conclusion with respect to photon production is that transverse expansion destroys

the correlation suggested in Ref. [15], so that T_c cannot be determined just from measurements of the shape of the single photon spectrum, as parametrized by T_{fit} . The monotonic dependence of T_{fit} on T_c is destroyed because the transverse flow increases as T_c decreases. However, the total production rate is also sensitive to T_c , so it is possible that comparison to the production rate instead of just the shape of the transverse momentum spectrum may be sufficient to determine T_c from data. In the transverse-momentum range studied, the inclusion of the a_1 resonance increases the photon yields by about 50%. Preliminary WA80 data appear to rule out large values for the equilibration time.

Chapter 4

Electron-Positron Pairs

4.1 Dilepton Production from Thermal Resonances

Dilepton pairs, such as e^+e^- (electron-positron pairs), are produced by, among other things, the decay of meson resonances such as the ρ^0 and ω within the hadron gas phase (mesons do not exist in the high-energy phase as their constituent quarks melt into the plasma). The invariant mass spectrum of e^+e^- pairs $dN_{e^+e^-}/dy$ is shown in Figure 4.1 on a logarithmic scale. It is the copious production of dileptons by resonances that allows us to view one type of production mechanism over the “background” when we look at the invariant mass spectrum of dilepton pairs coming out of a collision. For this reason, we focus our attention solely on resonance peaks in the experimental data and compare the model predictions to these data. Of particular interest is the NA45 experiment [4] which measured the invariant mass spectrum of e^+e^- pairs produced in 200 GeV/nucleon S+Au collisions. Because the measured spectrum includes a strong peak at around 775 MeV, I was able to compare the NA45 data to simulated results from decay of ρ^0 and ω mesons. The masses of the ρ^0 and ω , $m_\rho = 0.770$ GeV and $m_\omega = 0.780$ GeV, are too close to be separated experimentally [22], so we calculate the yields at the average mass of the ρ and ω , $m = 0.775$ GeV. The original idea to use e^+e^- transverse mass spectra as a thermometer for the QCD transition temperature [23] evolved through a model neglecting transverse expansion [24] to the current, more complete description [25].

The production of e^+e^- pairs from the collision is assumed to have two important parts, equilibrium and freeze-out. The equilibrium (also called “bulk”) contribution is calculated in the same way as the photon production in that we integrate over all the radial cells, each

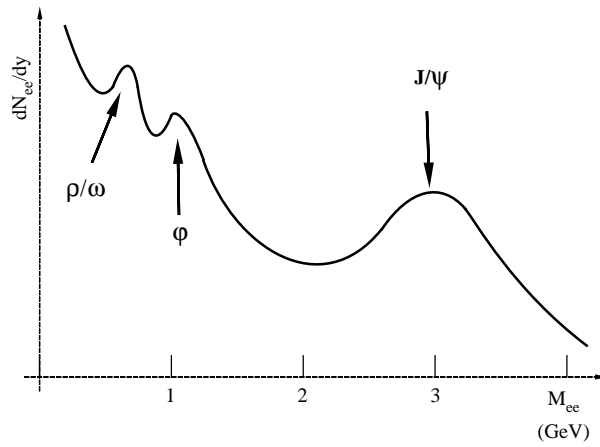


Figure 4.1: Schematic drawing of the invariant mass spectrum of e^+e^- pairs. The peaks, drawn on a log scale, are located at the masses of hadron resonances which have decay channels into e^+e^- pairs.

of which has a temperature and radial velocity, at each timestep throughout the history of the collision. We assume that there is a thermal population density of mesons in each cell, and these decay into e^+e^- pairs at a rate given by the partial widths of the mesons. The transverse mass distribution, which we calculate, is due to both the momentum distribution of the mesons in the rest frame of the fluid, and the fluid motion. Hence we expect to see that the apparent temperature of the spectrum is greater with radial expansion because of the transverse boost from the fluid motion. This is indeed what is seen for the bulk contribution to the spectrum.

The freeze-out contribution is more complicated. Below a certain “freeze-out” temperature T_{fo} , the mean free path of a meson is large enough that thermal equilibrium is no longer possible. Mesons that are found at these low temperatures stream freely toward the detectors, decaying on the way. Calculating this contribution requires calculating the motion of the freeze-out surface $T = T_{fo}$ ¹ and looking at the fluid just inside. In this fluid, there is still a thermal distribution of mesons. Some move outward, crossing the freeze-out surface toward the detectors. Others move inward, remaining in thermal equilibrium. The job is to compute the flow of mesons that make it across the freeze-out surface; a fraction of these, equal to the branching ratio, will decay into e^+e^- pairs.

Partial restoration of chiral symmetry in hot and dense matter [27] is expected to modify the masses and lifetimes (widths) of vector mesons. Changes in the ρ -meson properties may indicate chiral restoration through modified e^+e^- production. However, since it is not generally agreed upon how the in-medium ρ and ω masses behave [22] in nuclear matter, I took the vacuum masses and widths for my calculation. Arguments based on QCD sum rules [28] and effective Lagrangians [29] point to decreasing meson masses with increasing temperature and density, while vector-meson dominance studies [30] and consistency arguments [31] have been used to support the opposing view. I could have also taken a temperature-dependent width as in [32], but as is seen from the results, most of the e^+e^- pairs come from the lower-temperature fluid in the form of freeze-out, so the behavior of the width near the transition temperature T_c should not have much bearing on the results. For the time being, we therefore use the free mass and width of the resonances.

¹This is sometimes referred to as isothermal freeze-out. Other prescriptions (e.g. isochronous freeze-out [26]) are also possible.

4.2 Electron-positron Production from Equilibrium Matter

The production of e^+e^- pairs from the hot matter in equilibrium is calculated much like that of the single photons (Sect. 3.1). The spectra for massive particles are usually given in terms of the transverse mass, $m_T = \sqrt{p_T^2 + m^2}$, rather than the transverse momentum p_T . An integral for the total number of pairs N is written, and then the desired rapidity y and transverse mass m_T are filtered out with delta functions:

$$\left. \frac{d^2 N_{e^+e^-}^{(\rho^0+\omega)}}{m_T dm_T dy} \right|_{y=0} = \int_{-\infty}^{\infty} dy_f \int_{\tau_0}^{\infty} d\tau \tau \int_0^{\infty} dr 2\pi r \int_0^{\pi} d\theta \sin\theta \int_0^{2\pi} d\phi \int_0^{\infty} dp p^2 \frac{dR}{d^3p} \quad (4.1)$$

$$\times \delta\left(\frac{1}{2}m_T^2 - \frac{1}{2}m_T'^2\right) \delta\left(y_f + \tanh^{-1}\left[\frac{p \cos\theta}{\gamma(\sqrt{p^2 + m^2} + p v \sin\theta \cos\phi)}\right]\right) \Theta(T - T_{fo}).$$

Here R is the e^+e^- production rate per unit four-volume in the fluid frame, v is the transverse velocity of the fluid in the cell characterized by proper time τ , space-time (fluid) rapidity y_f and radial position r (measured in the frame moving with transverse velocity zero and longitudinal velocity $\tanh y_f$ in the lab), and $\gamma = (1 - v^2)^{-1/2}$.

For the e^+e^- production rate in the hadron gas phase, we assume that ρ and ω resonances are produced thermally in the equilibrium matter, and maintain a thermal population as some decay into e^+e^- pairs or other particles. One also keeps in mind that the decay rate, as viewed in the rest frame of the fluid, suffers time dilation due to the motion of the resonance with respect to the fluid. Hence the e^+e^- production rate for the thermally equilibrated hadron gas is

$$\frac{dR}{d^3p} = \frac{m(g_{\rho^0}\Gamma_{\rho^0 \rightarrow e^+e^-} + g_{\omega}\Gamma_{\omega \rightarrow e^+e^-})}{E(2\pi)^3} (e^{E/T} - 1)^{-1}, \quad (4.2)$$

where $g_{\rho^0} = g_{\omega} = 3$ are the spin degeneracies of the ρ^0 and ω mesons, and the partial widths are $\Gamma_{\rho^0 \rightarrow e^+e^-} = 6.77$ keV and $\Gamma_{\omega \rightarrow e^+e^-} = 0.60$ keV [33]. E is the energy measured in the fluid frame, and we use the average mass of the ρ and ω , $m = 0.775$ GeV. No mesons exist in the QGP, and hence the resonant e^+e^- production rate is zero for that part of the fluid.

As in the case of photons, (Sect. 3.1) the y_f integral is trivial, but for the integral over p , it is necessary to find an expression for p_* , the momentum of a meson in the fluid rest frame, in terms of the desired transverse momentum p_T . Applying a Lorentz boost in the

transverse direction to a meson with momentum p_* in the fluid frame gives

$$p_T^2 = \gamma^2 \left[v^2 (p_*^2 + m^2) + p_*^2 \sin^2 \theta \cos^2 \phi + 2v \sin \theta \cos \phi p_* \sqrt{p_*^2 + m^2} \right. \\ \left. + (1 - v^2) p_*^2 \sin^2 \theta \sin^2 \phi \right]. \quad (4.3)$$

One must invert this to get p_* as a function of m_T , the angles, and the fluid velocity v . This is done by rearranging and squaring both sides to give

$$4v^2 p_*^2 (p_*^2 + m^2) \sin^2 \theta \cos^2 \phi = \left[(1 - v^2) (m_T^2 - m^2) - v^2 (p_*^2 + m^2) \right. \\ \left. - p_*^2 \sin^2 \theta \cos^2 \phi - (1 - v^2) p_*^2 \sin^2 \theta \sin^2 \phi \right]^2, \quad (4.4)$$

which is a quadratic equation in p_*^2 . If both roots p_*^2 of (4.4) are complex or negative, then there is no physical solution and there is no contribution to the spectrum for that particular set of p_T , v , and angles θ and ϕ . If one or both roots is positive, then there may be solutions p_* that satisfy Eq. 4.3. Interpreting which roots make physical sense in the problem is left for Appendix C.2. The main point is that the integral over p is evaluated with the help of the delta functions much like the photon integral, with $p = p_*$ and $E = \sqrt{p_*^2 + m^2}$.

4.3 e^+e^- Pairs from Freeze-out

Below a certain freeze-out temperature, T_{fo} , the mesons' mean free paths are so long that they no longer stay in thermal equilibrium with the fluid, nor are they subject to the fluid motion as a whole; the frozen-out mesons travel freely toward the detectors until they decay. We model this as a sudden change which happens in the hadron gas phase, around 100-150 MeV, which is comparable to a pion mass. If we imagine that there is a “freeze-out surface” that moves in the radial direction (the x -axis in Figure 4.2; see explanation of axis labels in Sect. 2.1), then the thermal population of mesons on the immediate inside (hotter side) of the surface may partially flow through it. The flow of resonances through the surface is proportional to the difference between their velocity perpendicular to the surface, v_x , and the radial velocity of the freeze-out surface $dr/d\tau$, both viewed in the CM frame of the collision. Assuming the surface does not “catch up” with the mesons and swallow them up again, they will free-stream and a certain fraction of them, given by the branching ratio $\Gamma_{\rho^0(\omega) \rightarrow e^+e^-} / \Gamma_{\rho^0(\omega)}$ will decay into e^+e^- pairs. We assume there are no thermal resonances

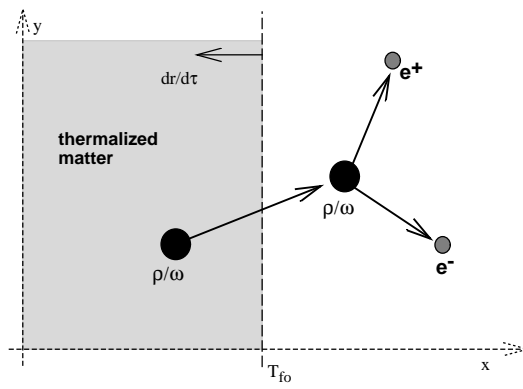


Figure 4.2: Freeze-out schematic.

on the outer side of the surface, so there is no flow if $v_x - dr/d\tau < 0$. The result for freeze-out production is

$$\begin{aligned} \left. \frac{d^2 N_{e^+e^-}^{(\rho+\omega)}}{m_T dm_T dy} \right|_{y=0} &= \left(\frac{g_{\rho^0} \Gamma_{\rho^0 \rightarrow e^+e^-}}{\Gamma_{\rho}} + \frac{g_{\omega} \Gamma_{\omega \rightarrow e^+e^-}}{\Gamma_{\omega}} \right) \int d\tau \tau 2\pi r(\tau) \int_{-1}^1 d(\cos \theta) \int_0^{2\pi} d\phi \quad (4.5) \\ &\times \int_0^{\infty} dp p^2 \gamma (2\pi)^{-3} \left(e^{E/T} - 1 \right)^{-1} \left(v_x - \frac{dr}{d\tau} \right) \Theta \left(v_x - \frac{dr}{d\tau} \right) \delta \left(\frac{1}{2} m_T^2 - \frac{1}{2} m'^2_T \right) \end{aligned}$$

where

$$v_x = \frac{p \sin \theta \cos \phi + v \sqrt{p^2 + m^2}}{\sqrt{p^2 + m^2} + p v \sin \theta \cos \phi} \quad (4.6)$$

is the component of the meson velocity perpendicular to the freeze-out surface, and $\Gamma_{\rho} = 151$ MeV and $\Gamma_{\omega} = 8.43$ MeV are the total widths for the ρ and ω [33]. $dr/d\tau$ is the radial velocity (evaluated numerically) of the freeze-out surface and $r(\tau)$ is its location. The Θ function ensures that only mesons going through the freeze-out surface in the outward direction are counted.

4.3.1 Freeze-out with No Transverse Expansion

For the calculations without transverse expansion, there is no radial dependence for any quantity (temperature, velocity, etc.). Therefore it makes no sense to talk about a freeze-out surface moving inward. In this case, there is an instantaneous freeze-out when the entire system, expanding longitudinally as in a pure Bjorken scenario, reaches the freeze-out temperature. All the mesons in the volume of the fluid stream freely towards the detectors, and decay on the way.

Let us call the time of freeze-out τ_{fo} . In the Bjorken picture, the entropy density falls as $1/\tau$. The freeze-out happens in the hadronic phase, so the freeze-out entropy is $s_{fo} = (4/3) c_h T_{fo}^3$. The total entropy per unit rapidity is (see Eq. B.9)

$$\frac{dS}{dy} = 3.6 \frac{dN_{\pi}}{dy} \quad , \quad (4.7)$$

and the volume per unit rapidity is

$$\frac{dV}{dy} = \pi R^2 \tau \quad . \quad (4.8)$$

From these the freeze-out time τ_{fo} can be calculated. To calculate the freeze-out spectrum, we start with

$$\frac{dN_{e^+e^-}}{dy} = (\pi R^2 \tau_{fo}) \left(\frac{g_{\rho^0} \Gamma_{\rho^0 \rightarrow e^+e^-}}{\Gamma_{\rho}} + \frac{g_{\omega} \Gamma_{\omega \rightarrow e^+e^-}}{\Gamma_{\omega}} \right) \int_0^{\infty} \frac{d^3p}{(2\pi)^3} f(E) \quad (4.9)$$

where g_{ρ^0} and g_{ω} are the degeneracies of the ρ^0 and ω mesons, and

$$f(E) = \left(e^{E/T_{fo}} - 1 \right)^{-1}, \quad (4.10)$$

is the population density of mesons with energy $E = \sqrt{p^2 + m^2}$. To get the contribution $dN_{e^+e^-}/m_T dm_T dy$ at a particular value of m'_T , a delta function $\delta(m_T^2/2 - m'^2_T/2)$ is inserted under the integral, as in Sect. 4.2.

4.4 Simulating Experimental Cuts

In any experiment, particularly a nuclear physics experiment with many particles reaching the detectors, it is necessary to filter the information to find the data of interest. In a given experiment, the raw data may include effects from sources other than the ones of interest, and the detectors always have limited ranges of sensitivity, resolution, etc. In the NA45 experiment [4], a few different kinds of cuts were made to select e^+e^- pairs in various invariant mass ranges and rapidity ranges. In our calculations we also implement cuts to take into account the limitations of the detectors.

4.4.1 Cut in Invariant Mass

The e^+e^- pairs were sorted into invariant mass bins of width 0.1 GeV, the ρ/ω peak falling into the 0.7-0.8 GeV bin. To simulate this cut in our calculation, we assumed a Breit-Wigner distribution for the individual ρ and ω peaks:

$$\frac{dN_{\rho^0 \rightarrow e^+e^-}}{dm^2 d\eta} = \left(\frac{dN_{\rho^0 \rightarrow e^+e^-}}{d\eta} \right) P_{\rho}(m^2), \quad (4.11)$$

where

$$P_{\rho}(m^2) = \frac{B(m_0/\Gamma_{\rho})m_0\Gamma_{\rho}}{(m^2 - m_0^2)^2 + m_0^2\Gamma_{\rho}^2}. \quad (4.12)$$

Normalization of the total distribution to unity gives

$$B\left(\frac{m_0}{\Gamma_\rho}\right) = \left[\frac{\pi}{2} + \arctan\left(\frac{m_0}{\Gamma_\rho}\right)\right]^{-1}. \quad (4.13)$$

A similar formula holds for e^+e^- pairs from ω decay.

To find the fraction of pairs of each species that would fall into the experimental bin, we integrate $P(m^2)$ from $m_1^2 = (0.7 \text{ GeV})^2$ to $m_2^2 = (0.8 \text{ GeV})^2$ giving

$$\int_{m_1^2}^{m_2^2} dm^2 P(m^2) = B\left(\frac{m_0}{\Gamma}\right) \left[\arctan\left(\frac{m_2^2 - m_0^2}{m_0 \Gamma}\right) - \arctan\left(\frac{m_1^2 - m_0^2}{m_0 \Gamma}\right) \right]. \quad (4.14)$$

We use $m_0 = 0.775 \text{ GeV}$, $\Gamma_\rho = 0.151 \text{ GeV}$, and $\Gamma_\omega = 8.43 \times 10^{-3} \text{ GeV}$ [33].

4.4.2 Cut in Rapidity

The mid-rapidity region in the experiment was taken to be $2.1 < (\eta \approx y) < 2.65$ in the lab frame, where η is the pseudorapidity, defined in Section 2.3. Both legs of the e^+e^- pair were required to fall in this range. For electrons and positrons produced by meson decay, whose mass is much less than their kinetic energy, we may use $\eta = y$. To get the fraction of pairs that survive this cut, we calculate the probability that a meson whose rapidity falls in this window decays into an e^+e^- pair which also falls into this window.

Let the rapidity window's width be $\Delta Y = 2.65 - 2.1 = 0.55$, and let the separation in rapidity of the emitted e^+e^- pair be δy . We assume that a meson may appear anywhere in the rapidity window with equal probability. Then the probability that both members of the e^+e^- pair fall in the window provided that the decaying meson was in the window is

$$f = \left[1 - \frac{\delta y}{\Delta Y}\right] \Theta(\Delta Y - \delta y). \quad (4.15)$$

This must be averaged over the angles θ and ϕ that one of the legs of the pair (the one with greater rapidity) can emerge with respect to the z and x axes, respectively. This average

depends on the radial velocity of the meson v as well, through δy 's dependence on v :

$$\langle f \rangle = \frac{\int_0^1 d(\cos \theta) \int_0^{2\pi} d\phi f(\delta y(\theta, \phi, v))}{\int_0^1 d(\cos \theta) \int_0^{2\pi} d\phi}. \quad (4.16)$$

δy can be expressed in terms of δv_z of one member as viewed by the other member of the pair,

$$\delta y = \frac{1}{2} \ln \left(\frac{1 + \delta v_z}{1 - \delta v_z} \right), \quad (4.17)$$

where

$$\delta v_z = \frac{2\gamma \cos \theta}{\gamma^2 (1 - v^2 \sin^2 \theta \cos^2 \phi) + \cos^2 \theta}. \quad (4.18)$$

Evaluating this gives a cut of about $\langle f \rangle = 0.13$ to 0.28 for the transverse mass range $0.795 \leq m_T \leq 2.755$.

4.4.3 Cut in Opening Angle

The NA45 experimenters [4] also employed a cut in opening angle to take into account the detectors limited resolution. All pairs with opening angle less than 35 mrad in the lab frame were rejected, as it is impossible to separate the paths at short distances from the meson decay location. This has a significant impact (a cut of more than 10^{-3} of the signal) only when m_T is well out of the range of transverse mass considered in this work.

4.5 Apparent Temperature of Dilepton Spectrum

As in the case of photon spectra, (Sect. 3.1) we want to fit an apparent temperature T_{fit} to the e^+e^- spectra we calculate. As the fitting procedure is supposed to be useful when applied to actual experimental data, we have filtered the simulated data before applying a fitting formula. An experimental measurement of an m_T spectrum from the $\rho - \omega$ peak would look at a finite range of m , so we filter the simulated data through an invariant mass bin of size $0.475 < m < 1.075$ GeV, assuming a Breit-Wigner distribution for each species. This range was chosen as a compromise between getting the entire ρ -peak and avoiding non-resonance contributions. As mentioned in section 4.4.2 a cut in pseudorapidity was

also applied, as in the NA45 experiment [4].

We take Eq. (4.1) and set $v = 0$ to simulate a Bjorken expansion [5] with no transverse expansion. The fitting formula obtained in [32] by this procedure is

$$\frac{d^2N_{e^+e^-}^{(\rho+\omega)}}{m_T dm_T dy} \sim \left(\frac{m_T}{T_{fit}}\right)^{1/2} \exp\left(-\frac{m_T}{T_{fit}} + 0.4 \frac{T_{fit}}{m_T}\right). \quad (4.19)$$

We extract the fit temperature, T_{fit} , by performing a least-squares fit to our calculated total spectrum (equilibrium plus freeze-out) in the window $1.155 \leq m_T \leq 1.755$ GeV, which is dominated by freeze-out. The part of the spectrum that is dominated by the equilibrium contribution is much smaller, typically $0.8 \leq m_T \leq 0.9$ GeV. Unfortunately this is of the order of a single experimental bin, so we choose instead to focus on the freeze-out contribution, in anticipation of fitting experimental data with both equilibrium and freeze-out contributions. As can be seen in Figure 4.3, the total spectrum exhibits different behavior in different m_T ranges. After some trial and error, we found that using the window where freeze-out is clearly dominant gave the most orderly and consistent results. In particular, the freeze-out apparent temperature measured in this window [25] gave a monotonic dependence of T_{fit} on T_c (see Sect. 4.6) for the range of collisions we studied.

4.6 Results

Our standard value for the equilibration time implies an initial temperature $T_0 = 327$ MeV with the value of dN/dy estimated for the NA45/CERES data (see Section 2.3). Fig. 4.3 shows the equilibrium (dash-dot) and freeze-out (short dash) contributions to the total $d^2N/m_T dm_T dy$ (full line) for a central S+Au collision at SPS energy for the standard parameter set with $T_c = 170$ MeV. The plot displays the features discussed at the end of the previous section (4.5).

In the absence of transverse expansion, T_{fit} is a monotonically increasing function, and comparable to T_c , so one can infer T_c given T_{fit} from the measured e^+e^- spectrum [24]. In Fig. 4.4, we vary T_c from 150 to 200 MeV and calculate the resulting values of T_{fit} while including transverse expansion. We find that T_{fit} is higher than in the case of longitudinal-only expansion, but still monotonic (except where T_{fo} approaches T_c). T_{fit} is 10-20 MeV lower for $\tau_0=1$ fm ($T_0=192$ MeV), which we attribute to the fact that transverse expansion develops relatively little in this case.

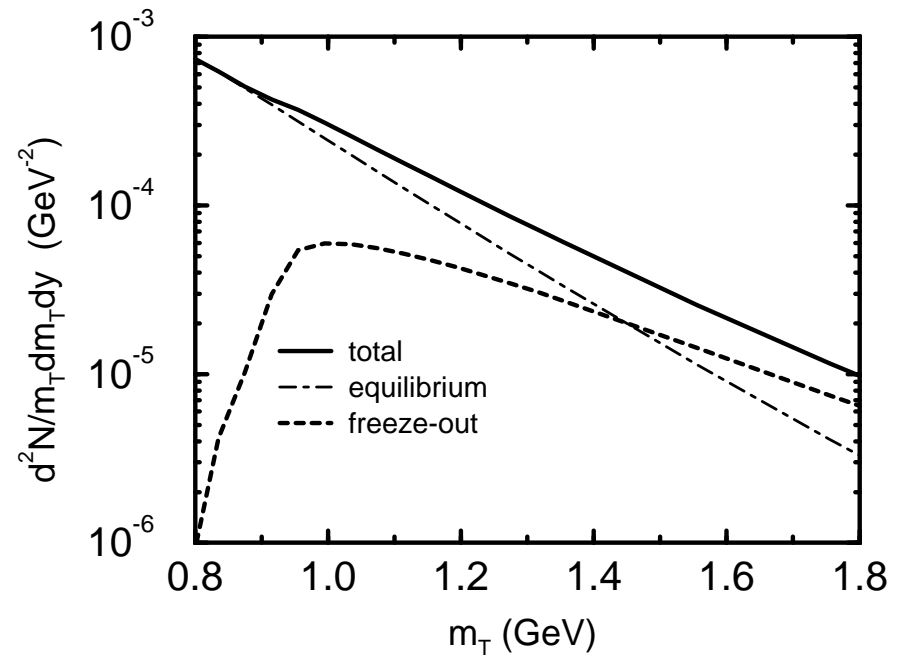


Figure 4.3: An example of the e^+e^- m_T -spectra in a central S+Au collision at SPS energy with the standard parameter set and $T_c = 170$ MeV.

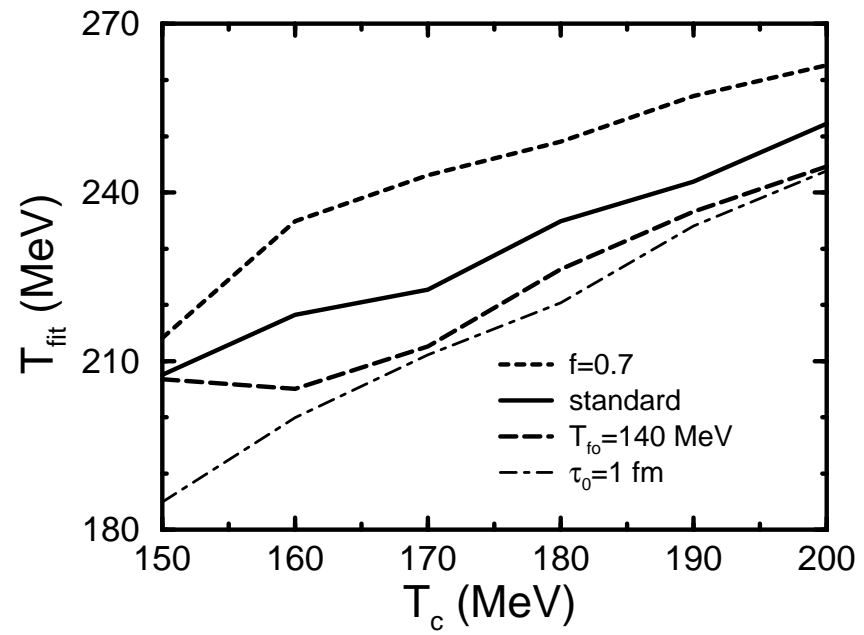


Figure 4.4: The apparent temperature T_{fit} for various parameter sets as a function of the transition temperature T_c .

We see that increasing T_{fo} to 140 MeV from its standard value decreases T_{fit} . For larger T_{fo} the hadronic matter near the freeze-out surface expands outward at a lower velocity, so that there is less contribution to m_T from the fluid motion. As T_{fo} approaches T_c , there is less motion at the freeze-out surface and the hadronic matter has less opportunity to shine, diminishing the role of the effect of fluid motion.

The curve for $f = 0.7$ shows that T_{fit} is about 15 MeV higher than for $f = 1$. The increase occurs because the temperature of the mixed phase, which makes a large contribution to the e^+e^- spectrum, is raised when f is lowered and B is held constant.

Our overall production rate underestimates by a factor of 1-3 the invariant mass spectrum measured by the NA45 experiment. We take the value measured in the experimental bin $0.7 < m < 0.8$ GeV (which contains the $\rho^0 - \omega$ peak), assuming that the signal is all from meson decay, obtaining $d^2N_{e^+e^-}^{(\rho^0+\omega)}/dmd\eta = 1.7 \times 10^{-3}$ GeV $^{-1}$. We calculate the same quantity for our simulated data from the standard calculation with $T_c=150$ MeV, including the experimental acceptance by counting only e^+e^- pairs whose members both have $2.1 < \eta < 2.65$, and integrating over a Breit-Wigner distribution for each species, giving us $d^2N_{e^+e^-}^{(\rho^0+\omega)}/dmd\eta = 5.9 \times 10^{-4}$ GeV $^{-1}$ for our standard parameter set. Increasing T_c to 200 MeV makes $d^2N_{e^+e^-}^{(\rho^0+\omega)}/dmd\eta = 1.2 \times 10^{-3}$ GeV $^{-1}$, still below the preliminary NA45/CERES data. Additional pair-producing processes not included here will increase the cross-section further. The overall production rate is sensitive to T_{fo} : increasing T_{fo} from 120 to 140 MeV while keeping $T_c = 150$ MeV gives $d^2N_{e^+e^-}^{(\rho^0+\omega)}/dmd\eta = 8.5 \times 10^{-4}$ GeV $^{-1}$ ($T_{fo} = 140$ MeV with $T_c = 200$ MeV gives $d^2N_{e^+e^-}^{(\rho^0+\omega)}/dmd\eta = 1.5 \times 10^{-3}$ GeV $^{-1}$); on the other hand, sensitivity to increasing τ_0 or decreasing f is minimal. Omitting transverse expansion gives a value that is at least a factor of 2-3 too high. Since the estimated error in the NA45 data is of order 50%, we would not rule out any of the calculations except that with no transverse expansion.

Chapter 5

Conclusions

We have, with a fluid dynamics code, calculated photon and e^+e^- spectra for a variety of heavy ion collision scenarios. A simple equation of state with a first-order phase transition was employed: a gas of massless pions in the low-temperature (hadronic) phase, and a gas of gluons and massless u and d quarks in the high-temperature (quark-gluon plasma) phase. The transition temperature T_c is adjustable, as is the freeze-out temperature T_{fo} . To simulate the effects of below-equilibrium quark densities, a parameter f , which varies between 0 (no quarks) and 1 (chemical equilibrium) is introduced. The thermalization time τ_0 , which is also the time when transverse expansion is allowed to begin, is also adjustable.

Photon and e^+e^- spectra were calculated with various values of the above-mentioned parameters. The results are displayed in Sections 3.3 and 4.6. The most important conclusions are summarized below.

Our conclusion with respect to photons is that for photons in $1 \text{ GeV} < p_T < 2 \text{ GeV}$, transverse expansion makes the $T_c - T_{fit}$ correlation double-valued for thermalization time $\tau_0 < 1.0 \text{ fm}/c$, so that T_c cannot be determined just from measurements of the shape of the single photon spectrum, as parametrized by T_{fit} . The monotonic dependence of T_{fit} on T_c is destroyed because the transverse flow increases as T_c decreases. This presents an obstacle for extracting T_c from measurements of the single photon spectra alone, and is a consequence of the increase in the importance of the transverse flow with decreasing T_c . Nevertheless, since the total photon yield increases monotonically with respect to T_c , using both the production rate and the shape of the transverse momentum spectrum may be sufficient for the determination of T_c from photon production.

The photon yields are sensitive to variations in the parameters. In the transverse-momentum range studied, the omission of the a_1 resonance decreases the photon yields by about 30%. Increasing the equilibration time to $\tau_0 = 1$ fm produces yields well above the preliminary WA80 data, which appears to rule out large values for the equilibration time.

Our most important conclusion with respect to e^+e^- production is that, in a carefully chosen fitting window, the correlation between T_c and T_{fit} is present even when the freeze-out contribution dominates. In contrast to the situation with photons, transverse expansion *does not* destroy the possibility of extracting T_c from the data with a judicious choice of the transverse mass window. The shape of the e^+e^- m_T spectrum, as parametrized by T_{fit} , should make a good thermometer to measure T_c .

Recent work by others [34] confirms the conjecture made by the NA45 experimenters [4] that the “excess” e^+e^- production is due to other hadronic processes, mainly $\pi\pi \rightarrow e^+e^-$. Adding these contributions to our calculated spectra may bring our results in line with the NA45 preliminary data for lower T_c calculations, which would increase confidence in our T_c estimation, as the WA80 data seem to favor lower T_c . Finally, even without this extra contribution to the calculated yields, omitting transverse expansion always overestimates the experimental data. Therefore, the preliminary NA45 data appear to definitely rule out models in which transverse expansion plays no role, and place constraints on other aspects of the collision dynamics.

Combining preliminary WA80 and NA45/CERES data on S+Au collisions at SPS energy we can say that the data do not favor long thermalization times and rule out scenarios in which transverse expansion plays no role. This is because transverse expansion hastens the cooling of the matter, greatly reducing the lifetime (or more accurately, the space-time volume) of the mixed phase, and hence the yields of any particles produced therein.

It is tempting to carry out a calculation like that in [20] without a transition to a high-energy phase in the present model. However, this would not be sensible with the massless pion gas approximation; the initial temperatures with so few degrees of freedom would be ridiculously high. Incorporating a realistic number of degrees of freedom would require that the complete resonance spectrum be taken into account, and such an investigation is beyond the scope of the present work.

We do not consider the effects of chemically-induced variations of particle density n in this work. Some authors have suggested that chemical equilibration in the initial QGP phase may take several times longer than thermal equilibrium [7, 8]; according to these

calculations, the hot matter that is created is made up almost entirely of gluons (Shuryak’s “hot glue” scenario [7]), with quark densities reaching only about half of their equilibrium value by the time transverse expansion begins. In this work, we attempted to approximate this effect by parametrizing the quark densities with a single variable f (Section 2.2). We plan to relax the assumption of chemical equilibrium in our fluid-dynamical calculation by explicitly calculating the chemistry that is coupled to the fluid dynamics. This will allow more realistic study of chemical non-equilibrium effects than was possible in the present work by parametrizing the departure from chemical equilibrium.

Some other improvements, with expected corrections on the 10% level, include considering the effects of a small but finite baryon number at central rapidity, and potential supercooling during the expansion of the mixed phase.

It is still unknown whether the transition from hadronic matter to QGP is first or higher order, though lattice QCD calculations place the width of the transition $\Delta T \leq 0.1 T_c$ [35]. The non-zero sound speed due to the finite transition width would introduce a pressure gradient during the transition, accelerating the expansion and reducing the yield of particles from later stages of the cooling.

It is of course necessary to calculate e^+e^- production at invariant masses other than $m_{\rho^0, \omega}$. For these calculations, one needs to calculate the production of pairs from processes other than resonance decay. The m_T spectra are very sensitive to fluid motion, and invariant mass m spectra are sensitive only to the temperature distributions. Combining information from both may provide more insight into evaluating fluid dynamical models. It will also be interesting to compare our results to Pb+Pb experiments in the near future when the Pb+Pb data become available.

Another suggestion [36] to measure T_c is to “tune” the beam energy to find the “softest point” of the EOS. Any imaginable technique would have to utilize a model, in which T_c is a parameter, for the temperature and velocity distributions of the created matter. We look upon the present work as providing such a model, and we expect it to prove generally useful in experimental work studying the QGP phase transition at RHIC.

Appendix A

Fluid Dynamic Details

For completeness, the conditions for stable shocks and rarefaction similarity waves are summarized in this appendix, based on existing literature [37]. In this work, we consider shocks and similarity solutions in one dimension, labeled “ x ”. This corresponds to the radial direction when we apply these one-dimensional solutions as an approximation to the cylindrically-symmetric geometry of the nuclear collision system.

A.1 Shocks and Stability

Shocks are most easily understood in the frame where the shock is at rest. In this frame, a stable shock discontinuity is surrounded by matter in a different state (w, v) on each side. For the shock to be stable, the flows of energy (T^{0x}) and of momentum (T^{xx}) must both be equal on the two sides. We use the notation $[A] \equiv A_R - A_L$ to denote the difference in the quantity A across the shock. Therefore, in the rest frame of the shock,

$$\begin{aligned} [T^{0x}] &= 0 , \\ [T^{xx}] &= 0 , \end{aligned} \tag{A.1}$$

where x is the spatial coordinate, 0 is the time coordinate, and the relativistically covariant stress-energy tensor is $T^{\mu\nu} = (e + P)u^\mu u^\nu - P g^{\mu\nu}$, with e being the energy density, P the pressure, u the four-velocity, and $g^{\mu\nu} = \text{diag}(1, -1, -1, -1)$ the metric tensor. Therefore $T^{00} = w\gamma^2 - P$, $T^{0x} = wv\gamma^2$, and $T^{xx} = wv^2\gamma^2 + P$.

If we transform Eqs. (A.1) into the frame where the shock is moving at velocity v_{sh} , we obtain

$$\begin{aligned} \left[\left(T^{x0} - v_{sh} (T^{xx} + T^{00}) + v_{sh}^2 T^{0x} \right) \gamma_{sh}^2 \right] &= 0 , \\ \left[\left(T^{xx} - v_{sh} (T^{x0} + T^{0x}) + v_{sh}^2 T^{00} \right) \gamma_{sh}^2 \right] &= 0 , \end{aligned} \quad (\text{A.2})$$

where $\gamma_{sh} \equiv 1/\sqrt{1 - v_{sh}^2}$. Multiplying each equation by v_{sh} and adding it to the other we obtain

$$\begin{aligned} \left[T^{x0} - v_{sh} T^{00} \right] &= 0 , \\ \left[T^{xx} - v_{sh} T^{0x} \right] &= 0 , \end{aligned} \quad (\text{A.3})$$

where, because of the symmetry of the stress-energy tensor, $T^{x0} = T^{0x} = wv\gamma^2$. A tiny bit of algebra reveals that this is the same as

$$\frac{[T^{0x}]}{[T^{00}]} = \frac{[T^{xx}]}{[T^{0x}]} = v_{sh} . \quad (\text{A.4})$$

In this work, the first equation of (A.4) is viewed as being a condition necessary for a stable shock, and the value of v_{sh} being the result of the particular values of w and v used on the two sides to satisfy the shock condition.

A special case arises when the shock is in mixed phase matter. In the mixed phase, the pressure is a constant, P_c , regardless of the energy density, and therefore the sound speed $c_s = 0$. If we explicitly write out Eqs. (A.1) in terms of w , v , and P , we get

$$\begin{aligned} [T^{0x}] &= 0 \implies w_L v_L \gamma_L^2 = w_R v_R \gamma_R^2 , \\ [T^{xx}] &= 0 \implies w_L v_L^2 \gamma_L^2 + P_L = w_R v_R^2 \gamma_R^2 + P_R . \end{aligned} \quad (\text{A.5})$$

If both the left and right side are made of mixed phase matter, $P_L = P_R$, so we obtain

$$\begin{aligned}
w_L v_L (1 - v_R^2) &= w_R v_R (1 - v_L^2) , \\
w_L v_L^2 (1 - v_R^2) &= w_R v_R^2 (1 - v_L^2) .
\end{aligned}
\tag{A.6}$$

Dividing the second equation of (A.6) by the first shows that this is only true if $v_L = v_R$. Note that w_L and w_R must be finite because we have already specified that they are in the mixed phase. Thus the requirement for a shock in the mixed phase to be stable is that the velocity of the fluid is continuous across the shock. The shock velocity, as measured in an arbitrary inertial frame, is calculated for the special case of mixed phase matter:

$$v_{sh} = \frac{[T^{0x}]}{[T^{00}]} = \frac{w_L v_L \gamma_L^2 - w_R v_R \gamma_R^2}{w_L \gamma_L^2 - P_L - w_R \gamma_R^2 + P_R} .
\tag{A.7}$$

Because in the mixed phase $P_L = P_R$, and we derived that $v_L = v_R$ in the rest frame of the shock, we can write

$$v_{sh} = \frac{v \gamma^2 (w_L - w_R)}{\gamma^2 (w_L - w_R)} = v ,
\tag{A.8}$$

where v is the velocity of the fluid on both sides of the shock. So we see that the shock moves along with the fluid, as we might expect if we consider that there is no pressure difference across the shock.

A.2 Rarefaction Waves

The other non-trivial type of flow pattern is the rarefaction wave. A rarefaction wave joins regions of different densities by varying the density and velocity smoothly between two positions. In this section we derive the differential equation for a rarefaction wave, assuming it has no length or time scale, i.e. is a similarity pattern.

Similarity patterns depend on position only through the variable $\chi \equiv x/t$. We can write the derivatives with respect to x and t as:

$$\begin{aligned}
\frac{d}{dt} &= \left(\frac{d\chi}{dt} \right) \frac{d}{d\chi} = \left(\frac{-\chi}{t} \right) \frac{d}{d\chi} , \\
\frac{d}{dx} &= \left(\frac{d\chi}{dx} \right) \frac{d}{d\chi} = \left(\frac{1}{t} \right) \frac{d}{d\chi} .
\end{aligned}
\tag{A.9}$$

We can then rewrite the conservation laws expressed by $\partial_\mu T^{\mu\nu} = 0$ as

$$\begin{aligned} -\chi \left(\frac{dT^{00}}{d\chi} \right) + \frac{dT^{x0}}{d\chi} &= 0 , \\ -\chi \left(\frac{dT^{0x}}{d\chi} \right) + \frac{dT^{xx}}{d\chi} &= 0 . \end{aligned} \tag{A.10}$$

Putting in the explicit form of the tensor elements (see Sect. A.1) we obtain

$$\begin{aligned} (v - \chi)\gamma^2 \frac{dw}{d\chi} + \chi \frac{dP}{d\chi} + w(v^2 - 2v\chi + 1)\gamma^4 \frac{dv}{d\chi} &= 0 , \\ v(v - \chi)\gamma^2 \frac{dw}{d\chi} + \frac{dP}{d\chi} + w(-v^2\chi + 2v - \chi)\gamma^4 \frac{dv}{d\chi} &= 0 . \end{aligned} \tag{A.11}$$

In this work we deal with an equation of state (Sect. 2.2) in which P depends only on the energy density e (or equivalently, the enthalpy density $w = e + P$), so the sound speed is $c_s^2 = dP/de$. We then have

$$\frac{dP}{d\chi} = \left(\frac{c_s^2}{1 + c_s^2} \right) \frac{dw}{d\chi} . \tag{A.12}$$

We can use this to rewrite Eqs. (A.11) as

$$\begin{aligned} \frac{1}{w} \frac{dw}{d\chi} &= \frac{(v^2 - 2v\chi + 1)\gamma^2(1 + c_s^2)}{c_s^2 v^2 \chi - (1 + c_s^2)v + \chi} \frac{dv}{d\chi} , \\ \frac{1}{w} \frac{dw}{d\chi} &= \frac{(v^2 - 2v + \chi)\gamma^2(1 + c_s^2)}{v^2 - (1 + c_s^2)v\chi + c_s^2} \frac{dv}{d\chi} . \end{aligned} \tag{A.13}$$

For both of these to be true, either

$$\frac{dw}{d\chi} = \frac{dv}{d\chi} = 0 , \tag{A.14}$$

which describes a uniform region, or

$$\chi = \frac{v \pm c_s}{1 \pm v c_s} . \quad (\text{A.15})$$

This describes a (similarity) rarefaction wave, in which a part of the pattern with a given enthalpy density w and fluid velocity v , whose position is described by χ , moves at the speed of sound c_s with respect to the fluid (note the relativistic velocity addition formula). When the more dense part of the wave is towards negative χ , as it is in this work, the \pm sign becomes a minus sign, meaning the rarefaction moves to the left.

We can substitute into Eqs. (A.13) the expression for v in terms of χ , and solve to obtain

$$\frac{1}{w} \frac{dw}{d\chi} = \frac{1 + c_s^2}{\pm c_s (1 - \chi^2)} , \quad (\text{A.16})$$

which can be integrated to give

$$\ln w = \pm \frac{1}{2} \left(\frac{1 + c_s^2}{c_s} \right) \ln \left(\frac{1 + \chi}{1 - \chi} \right) + \text{const.} \quad (\text{A.17})$$

for an equation of state with a constant sound speed c_s . We can exponentiate this and substitute in $\chi(v)$ to get

$$w = \text{const.} \times \left(\frac{1 + v}{1 - v} \right)^{\pm(1+c_s^2)/2c_s} . \quad (\text{A.18})$$

For the equation of state of hadronic and quark matter used in this work, $c_s = 1/\sqrt{3}$, and $(1 + c_s^2)/2c_s = 2/\sqrt{3}$. For mixed-phase matter $c_s = 0$, so the rarefaction wave would be infinitely steep, i.e. a shock. Shocks, including the special case for mixed-phase matter, are discussed in Section A.1.

Appendix B

Math: Equation of State

B.1 Entropy of Pions

In this section I calculate the entropy per particle for massless pions. As discussed in Section 2.2, the entropy density $s = w/T$, where $w = e + P$ is the enthalpy density, and T is the temperature. All we need to do is calculate w and the particle density n .

As shown in Section 2.2, $w = 4e/3$, where $e = (3\pi^2/30)T^4$. The number density n is calculated much like the energy in Sect. 2.2:

$$n(T) = 3 \frac{4\pi}{(2\pi)^3} \int_0^\infty dk k^2 \frac{1}{\exp(\beta k) - 1} . \quad (\text{B.1})$$

Here we go into more detail about evaluating the integral. We expand the integrand in powers of $e^{-\beta k}$:

$$\begin{aligned} \frac{k^2}{\exp(\beta k) - 1} &= k^2 e^{-\beta k} [1 + e^{-\beta k} + e^{-2\beta k} + e^{-3\beta k} + \dots] \\ &= \sum_{n=1}^{\infty} k^2 e^{-n\beta k} . \end{aligned} \quad (\text{B.2})$$

We can make the variable substitution $x = \beta k$, so that $k = Tx$ and we get

$$I \equiv \int_0^\infty dk \frac{k^2}{\exp(\beta k) - 1} = T^3 \int_0^\infty dx \sum_{n=1}^{\infty} x^2 e^{-nx} , \quad (\text{B.3})$$

and from a table of integrals [38],

$$\int_0^\infty dx x^2 e^{-nx} = \frac{2!}{n^{2+1}} = \frac{2}{n^3} . \quad (\text{B.4})$$

We now need to evaluate the sum

$$I = 2T^3 \sum_{n=1}^{\infty} \frac{1}{n^3} . \quad (\text{B.5})$$

This can be evaluated either through contour integration [9] or by looking in a table for the numerical value [38]. We find that

$$I = 2T^3 \sum_{n=1}^{\infty} \frac{1}{n^3} = 2(1.20206) T^3 , \quad (\text{B.6})$$

$$n(T) = 6 \frac{4\pi}{(2\pi)^3} (1.20206) T^3 .$$

Similarly,

$$w(T) = \frac{4}{3} (3) \frac{4\pi}{(2\pi)^3} \int_0^\infty dk k^2 \frac{k}{\exp(\beta k) - 1} , \quad (\text{B.7})$$

and we expand the integrand as in Eq. (B.2) to obtain

$$\begin{aligned} w(T) &= \frac{4}{3} (3) \frac{4\pi}{(2\pi)^3} (6) T^4 \sum_{n=1}^{\infty} \frac{1}{n^4} \\ &= \frac{4}{3} (3) \frac{4\pi}{(2\pi)^3} (6) (1.08232) T^4 . \end{aligned} \quad (\text{B.8})$$

The end result for the entropy per particle is

$$\frac{s}{n} = \frac{w/T}{n} = \frac{(4/3)(3)(6)(1.08232) T^3}{(6)(1.20206) T^3} = 3.6 . \quad (\text{B.9})$$

B.2 The 7/8 Factor

In Section 2.2 it was mentioned that

$$\int_0^\infty dk k^2 \frac{k}{e^{\beta k} + 1} = \frac{7}{8} \int_0^\infty dk k^2 \frac{k}{e^{\beta k} - 1} . \quad (\text{B.10})$$

This can be demonstrated without actually fully evaluating the integrals. Generalizing from Eqs. (B.2) and (B.3),

$$\frac{k^3}{e^{\beta k} - 1} = T^3 \sum_{n=1}^{\infty} x^3 e^{-nx} , \quad (\text{B.11})$$

where we have made the variable substitution $x = \beta k$. Similarly,

$$\begin{aligned} \frac{k^3}{e^{\beta k} + 1} &= T^3 \frac{x^3}{e^x + 1} \\ &= T^3 \frac{e^{-x} x^3}{e^{-x} + 1} \\ &= T^3 e^{-x} x^3 \left[1 - e^{-x} + e^{-2x} - e^{-3x} + \dots \right] \\ &= T^3 \sum_{n=1}^{\infty} x^3 e^{-nx} (-1)^{n+1} \\ &= T^3 \left[\sum_{n=1}^{\infty} x^3 e^{-nx} - 2 \sum_{n=1}^{\infty} \left(\frac{u}{2}\right)^3 e^{-nu} \right] \\ &= T^3 \left[\sum_{n=1}^{\infty} x^3 e^{-nx} - \frac{1}{4} \sum_{n=1}^{\infty} u^3 e^{-nu} \right], \end{aligned} \quad (\text{B.13})$$

where I have made the variable substitution $u = 2x$. Integrating expression (B.13) over x we get

$$\begin{aligned} &T^3 \int_0^{\infty} dx \left[\sum_{n=1}^{\infty} x^3 e^{-nx} - \frac{1}{4} \sum_{n=1}^{\infty} u^3 e^{-nu} \right] \\ &= T^3 \left[\int_0^{\infty} dx \sum_{n=1}^{\infty} x^3 e^{-nx} \right] - \left[\frac{1}{8} \int_0^{\infty} du \sum_{n=1}^{\infty} u^3 e^{-nu} \right] \\ &= \frac{7}{8} T^3 \left[\int_0^{\infty} dx \sum_{n=1}^{\infty} x^3 e^{-nx} \right]. \end{aligned} \quad (\text{B.14})$$

Comparing expression (B.14) with Eqs. (B.3) and (B.10) we see that we get the stated result.

Appendix C

Math: Miscellaneous

C.1 Corrections to Pressure Estimate

Earlier (Sect. 2.4) I mentioned that we approximate the pressure integral using only the original value of the pressure P_0 . Here I show that this is sufficient if the calculation is to order $\delta\tau$.

Suppose we estimate P_{new} in terms of a differential away from P_0 . Let

$$\Delta P = P_{new} - P_0 = P(\Theta^{00}, \Theta^{0r}) - P(\Theta_0^{00}, \Theta_0^{0r}) = d\Theta^{00} \frac{\partial P}{\partial \Theta^{00}} + d\Theta^{0r} \frac{\partial P}{\partial \Theta^{0r}} \quad (\text{C.1})$$

where the partial derivatives of P are evaluated at the current values of the tensor elements, and $d\Theta^{\mu\nu} = \Theta_{new}^{\mu\nu} - \Theta_0^{\mu\nu}$. We can re-write the first equation of (2.29) using this estimate for the average P :

$$(\tau + \delta\tau)\Theta_{new}^{00} = \tau\Theta_0^{00} - \frac{\delta\tau^2 + 2\tau\delta\tau}{\delta r^2 + 2r\delta r} [(r + \delta r)T_+^{0r} - rT_-^{0r}] + \delta\tau \left(P_0 + \frac{1}{2}\Delta P \right). \quad (\text{C.2})$$

The second equation of (2.29) is treated in a similar manner.

The corrected versions of Eqs. (2.29) can then be rearranged as a linear system in the differentials $d\Theta^{00}$ and $d\Theta^{0r}$,

$$a d\Theta^{00} + b d\Theta^{0r} = e, \quad (\text{C.3})$$

$$c d\Theta^{00} + d d\Theta^{0r} = f,$$

where a, b, c, d, e and f are knowns. The system of equations is solved by matrix inversion, and terms of order $\delta\tau$ are kept. This gives us

$$\begin{aligned} d\Theta^{00} &= \frac{\delta\tau}{\tau} \left[\frac{2\tau}{\delta r^2 + 2r\delta r} \left[(r + \delta r) T_+^{0r} - r T_-^{0r} \right] + P_0 - \Theta_0^{00} \right], \quad (\text{C.4}) \\ d\Theta^{0r} &= \frac{\delta\tau}{\tau} \left[\frac{2\tau}{\delta r^2 + 2r\delta r} \left[(r + \delta r) T_+^{rr} - r T_-^{rr} \right] + \frac{2\tau}{\delta r + 2r} P_0 - \Theta_0^{0r} \right]. \end{aligned}$$

These can be re-arranged into a directly-applicable form like Eqs. (2.29). For illustration, I work out the Θ^{00} case.

$$\begin{aligned} d\Theta^{00} &= \frac{\delta\tau}{\tau} \left[\frac{2\tau}{\delta r^2 + 2r\delta r} \left[(r + \delta r) T_+^{0r} - r T_-^{0r} \right] + P_0 - \Theta_0^{00} \right], \quad (\text{C.5}) \\ \tau\Theta^{00} - \tau\Theta_0^{00} &= \delta\tau \left[\frac{2\tau}{\delta r^2 + 2r\delta r} \left[(r + \delta r) T_+^{0r} - r T_-^{0r} \right] + P_0 - \Theta_0^{00} \right], \\ \tau\Theta^{00} &= (\tau - \delta\tau)\Theta_0^{00} + \frac{2\tau\delta\tau}{\delta r^2 + 2r\delta r} \left[(r + \delta r) T_+^{0r} - r T_-^{0r} \right] + \delta\tau P_0. \end{aligned}$$

Multiplying through by $\tau/(\tau - \delta\tau)$ reveals that this is the same as the first equation of (2.29) to first order in $\delta\tau$. The same procedure is done on the other ‘‘corrected’’ equation, and that also matches the original to first order in $\delta\tau$.

C.2 Interpretation of Roots of Eq. 4.4

In Section 4.1 we had gotten as far as Eq. (4.4),

$$\begin{aligned} 4v^2 p_*^2 (p_*^2 + m^2) \sin^2 \theta \cos^2 \phi &= \left[(1 - v^2) (m_T^2 - m^2) - v^2 (p_*^2 + m^2) \right. \\ &\quad \left. - p_*^2 \sin^2 \theta \cos^2 \phi - (1 - v^2) p_*^2 \sin^2 \theta \sin^2 \phi \right]^2, \quad (\text{C.6}) \end{aligned}$$

a quadratic equation in p_*^2 . We still need to solve for p_* , the momentum in the fluid frame, given a measured m_T (or p_T) in the CM frame. This section is concerned with finding which solutions for p_* are physically sensible.

Given a real solution for p_*^2 , we can immediately eliminate negative p_* as unphysical; so the problem is reduced to finding which of the two solutions for p_*^2 is or are valid. We can draw a diagram that will help us visualize the roots physically (see Fig. C.1). If, as before

(Sect. 2.1), we imagine the x -axis as the radial direction in our system, and $p_T^2 = p_x^2 + p_y^2$, then we can draw a circle in momentum space that represents the desired p_T . We can draw a point on the p_x -axis and let this represent the momentum of a resonance that is at rest with respect to the fluid; thus the fluid velocity is mapped onto the p_x axis. If a vector \mathbf{p}_* is drawn starting from such a point, then vector \mathbf{p}' (see Fig. C.1) represents the momentum of the resonance viewed in the CM frame. Of course, this should be done relativistically, so our Galilean picture is somewhat distorted, but it does illustrate the point. Note that there is no representation of p_z in the diagram as it has no bearing on p_T .

Now, for a given fluid velocity v and the angles θ and ϕ (measured in the fluid frame) we are asked to solve for $|\mathbf{p}_*|$ that results in a given p_T . This is easy to see on the diagram: the fluid velocity is represented by where a point lies on the p_x axis, and the angle ϕ is represented by the angle of the vector \mathbf{p}_* in the diagram. The angle θ is represented by the $\sin \theta$ scaling of \mathbf{p}_* ; the z -axis goes into the plane of the picture. It is easy to see that if $mv\gamma < p_T$ (see Fig. C.1) then there is exactly one (positive) solution for p_* , and if $mv\gamma > p_T$ (see Fig. C.2) then there are either zero or two solutions, depending on the angles. While it may seem that the availability of two solutions for a given set of angles would mean a sudden jump in production if $mv\gamma$ increases infinitesimally above p_T , a closer inspection will show that fluid velocities inside the circle always have a solution for $\phi \rightarrow \phi + \pi$, whereas outside the circle this is never true. Therefore the overall pair production from a parcel of fluid is continuous with respect to the fluid velocity.

Inside the circle ($mv\gamma < p_T$), where there is only one solution for p_* , one takes the root of the quadratic equation with the smaller (larger) magnitude if $\cos \phi$ is positive (negative). Alternatively, we can take the positive square root of p_*^2 and check if it is consistent with the original Lorentz transform, Eq. (4.3). Outside the circle, this must be done anyway, even if the determinant is non-negative; a non-negative determinant means only that there exists values of p_*^2 that satisfy Eq. (C.6), not that the positive roots $p_* = +\sqrt{p_*^2}$ satisfy Eq. (4.3).

The solutions used by the code are then, for $mv\gamma < p_T$,

$$B \cos \phi > 0 : p_*^2 = \frac{-B + \sqrt{B^2 - 4AC}}{2A} , \quad (\text{C.7})$$

$$B \cos \phi < 0 : p_*^2 = \frac{-B - \sqrt{B^2 - 4AC}}{2A} , \quad (\text{C.8})$$

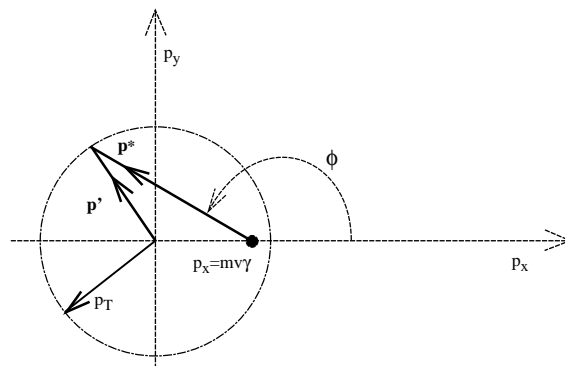


Figure C.1: When there is exactly one solution for p_* .

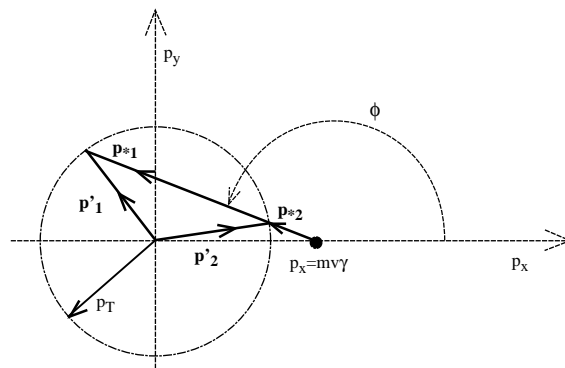


Figure C.2: When there are two solutions for p_* .

where

$$\begin{aligned}
A &= 4v^2 \sin^2 \theta \cos^2 \phi - \left(v^2 + \sin^2 \theta - v^2 \sin^2 \theta + v^2 \sin^2 \theta \cos^2 \phi \right)^2, \\
B &= 4v^2 m^2 \sin^2 \theta \cos^2 \phi + 2 \left(m_T^2 - m^2 - v^2 m_T^2 \right) \left(v^2 + \sin^2 \theta - v^2 \sin^2 \theta + v^2 \sin^2 \theta \cos^2 \phi \right), \\
C &= - \left(m_T^2 - m^2 - v^2 m_T^2 \right)^2.
\end{aligned} \tag{C.9}$$

For $mv\gamma > p_T$, where either or both solutions may be valid, we use both formulae, but check to make sure that $+\sqrt{p_*^2}$ satisfies Eq. (4.3).

We can now evaluate the sub-integral over p in either Eq. (4.1) or (4.5). Note that

$$\delta \left(\frac{1}{2} m_T^2 - \frac{1}{2} m_T'^2 \right) = \delta \left(\frac{1}{2} p_T^2 - \frac{1}{2} p_T'^2 \right), \tag{C.10}$$

because $m_T = \sqrt{m^2 + p_T^2}$. We rewrite the delta function,

$$\delta \left(\frac{1}{2} m_T^2 - \frac{1}{2} m_T'^2 \right) = \sum_{p_*} \frac{\delta(p - p_*)}{|K|_{p=p_*}}, \tag{C.11}$$

where

$$\begin{aligned}
K = \frac{1}{2} \frac{\partial p_T^2}{\partial p} &= \gamma^2 \left[p \left(v^2 + \sin^2 \theta - v^2 \sin^2 \theta + v^2 \sin^2 \theta \cos^2 \phi \right) \right. \\
&\quad \left. + v \sin \theta \cos \phi \sqrt{p^2 + m^2} + \frac{p^2 v \sin \theta \cos \phi}{\sqrt{p^2 + m^2}} \right].
\end{aligned} \tag{C.12}$$

We are left with

$$\int_0^\infty dp p^2 \left(\frac{dR}{d^3 p} \right) \delta \left(\frac{1}{2} m_T^2 - \frac{1}{2} m_T'^2 \right) = \sum_{p_*} \frac{p_*^2}{|K|_{p=p_*}} \left(\frac{dR}{d^3 p} \right)_{E=\sqrt{p_*^2+m^2}} \tag{C.13}$$

where the sum is over all solutions for p_* .

Bibliography

- [1] C.M. Hung and E.V. Shuryak, Phys. Rev. Lett. **75**, 4003 (1995).
- [2] C.-Y. Wong, *Introduction to High-Energy Heavy-Ion Collisions*, World Scientific Publishing Co., 1994.
- [3] R. Santo *et al.*, Nucl. Phys. **A566**, 61c (1994).
- [4] G. Agakichiev *et al.*, CERES Collaboration, Phys. Rev. Lett. **75**, 1272 (1995); T. Ullrich, private communication.
- [5] J.D. Bjorken, Phys. Rev. D **27**, 140 (1983).
- [6] NA35 Collaboration, D. Roehrich *et al.*, Nucl. Phys. **A566**, 35c (1994).
- [7] E. Shuryak, Phys. Rev. Lett. **68**, 3270 (1992).
- [8] K. Geiger and J.I. Kapusta, Phys. Rev. D **47**, 4905 (1993).
- [9] F. Reif, *Fundamentals of Statistical and Thermal Physics*, McGraw-Hill Book Company, 1965.
- [10] A. Chodos, R.L. Jaffe, K. Johnson, C.B. Thorn and V. Weisskopf, Phys. Rev. D **9**, 3471 (1974); A. Chodos, R.L. Jaffe, K. Johnson, and C.B. Thorn, Phys. Rev. D **10**, 2599 (1974);
- [11] J.-P. Blaizot and J.-Y. Ollitrault, Nucl. Phys. **A458**, 745 (1986).
- [12] V. Schneider *et al.*, Journal of Computational Physics **105**, 92 (1993); D.H. Rischke, Columbia preprint CU-TP-692.
- [13] J.J. Neumann, D. Seibert, and G. Fai, Phys. Rev. C **51**, 1460 (1995).

- [14] J. Kapusta, P. Lichard and D. Seibert, Phys. Rev. D **44**, 2774 (1991).
- [15] D. Seibert, Z. Phys. **C58**, 307 (1993).
- [16] J.I. Kapusta, *Finite Temperature Field Theory* (Cambridge University Press, Cambridge, England, 1989).
- [17] H. Nadeau, J. Kapusta and P. Lichard, Phys. Rev. C **45**, 3034 (1992).
- [18] L. Xiong, E. Shuryak, and G.E. Brown, Phys. Rev. D **46**, 3798 (1992).
- [19] C. Song, Phys. Rev. C **47**, 2861 (1993).
- [20] D.K. Srivastava and B. Sinha, Phys. Rev. Lett. **73**, 2421 (1994).
- [21] E. Shuryak and L. Xiong, Phys. Lett. B **333**, 316 (1994).
- [22] R. Pisarski, Nucl. Phys. **A590**, 553c (1995).
- [23] D. Seibert, Phys. Rev. Lett. **68**, 1476 (1992).
- [24] D. Seibert, V. Mishra, and G. Fai, Phys. Rev. C **46**, 330 (1992).
- [25] J.J. Neumann, D. Seibert, and G. Fai, Phys. Rev. C **53**, R14 (1996).
- [26] S. Bernard, J.A. Maruhn, W. Greiner, and D.H. Rischke, Frankfurt preprint UFTP-406, Columbia preprint CU-TP-733, 1996.
- [27] G.Q. Li, C.M. Ko, Nucl. Phys. **A582**, 731 (1995).
- [28] T. Hatsuda and S.H. Lee, Phys. Rev. C **46**, R34 (1992).
- [29] H.C. Jean, J. Piekarewicz and A.G. Williams, Phys. Rev. C **49**, 1981 (1994).
- [30] C. Gale and J. Kapusta, Nucl. Phys. B **357**, 65 (1991).
- [31] J. Ellis, J.I. Kapusta and K.A. Olive, Phys. Lett. B **273**, 123 (1991).
- [32] D. Seibert, Phys. Rev. Lett. **68**, 1476 (1992); D. Seibert, V.K. Mishra, and G. Fai, Phys. Rev. C **46**, 330 (1992).
- [33] *Review of Particle Properties*, Phys. Rev. **D50**, 1173 (1994).

- [34] G. Chanfray, R. Rapp, and J. Wambach, Phys. Rev. Lett. **76** 368 (1996).
- [35] D.H. Rischke and M. Gyulassy, Columbia Univ. preprint CU-TP-706 (1995) and references therein.
- [36] C.M. Hung and E.V. Shuryak, Phys. Rev. Lett. **75** 4003 (1995).
- [37] D. Seibert, Ph.D. dissertation, University of Illinois at Urbana-Champaign, 1988.
- [38] *CRC Standard Mathematical Tables*, Fifteenth Edition, The Chemical Rubber Co., 1967.